

# Bow shocks, bow waves, and dust waves

William J. Henney, S. Jane Arthur, & Jorge A. Tarango-Yong

*Instituto de Radioastronomía y Astrofísica, Universidad Nacional Autónoma de México, Apartado Postal 3-72, 58090 Morelia, Michoacán, México*

Accepted XXX. Received YYY; in original form ZZZ

## ABSTRACT

Dust waves and bow waves result from the action of a star’s radiation pressure on a stream of dust grains that is flowing past it. They are an alternative mechanism to hydrodynamic bow shocks for explaining the curved arcs of infrared emission seen around some stars. We employ simple cylindrically symmetric models for the dust grain dynamics under the influence of radiation and weak gas–grain coupling, which produce bow shapes that we call dragoids. We also show how thin-shell hydrodynamic models can be modified to treat the case of strong gas-grain coupling, producing bow shapes that we call trapoids. Using our recently developed two-dimensional classification scheme for projected bow shapes, we then analyze the inclination-dependent tracks of the dragoids and trapoids in the planitude–alatitude plane, finding interesting differences from the wilkinoid, cantoid, and ancantoid shapes of hydrodynamic bow shock models. We further show how these are modified in the presence of small-amplitude standing-wave oscillations of the basic shape, as may be produced by hydrodynamic instabilities or a time-varying source. We analyze the prospects of using shape analysis of observational datasets to discriminate between different bow models, finding that sample sizes of order 100 are required.

**Key words:** circumstellar matter – radiation: dynamics – stars: winds, outflows

## 1 INTRODUCTION

Curved emission arcs around stars (e.g., Gull & Sofia 1979) are often interpreted as *bow shocks*, due to a supersonic hydrodynamic interaction between the star’s wind and an external stream. This stream may be due to the star’s own motion or to an independent flow, such as an H II region in the champagne phase (Tenorio-Tagle 1979), or another star’s wind (Canto et al. 1996). However, an alternative interpretation in some cases may be a radiation-pressure driven bow wave, as first proposed by van Buren & McCray (1988, §vi). In this scenario, photons emitted by the star are absorbed by dust grains in the incoming stream, with the resultant momentum transfer being sufficient to decelerate and deflect the grains within a certain distance from the star, forming a dust-free, bow-shaped cavity with an enhanced dust density at its edge. Two regimes are possible, depending on the strength of coupling between the gas (or plasma) and the dust. In the strong-coupling regime, gas–grain drag decelerates the gas along with the dust, forming a shocked gas shell in a similar fashion to the wind-driven bow shock case. In the weak-coupling regime, the gas stream is relatively unaffected and the dust temporarily decouples to form a dust-only shell. This second case has recently been studied in detail in the context of the interaction of late O-type stars (which have only weak stellar winds) with dusty photoevaporation flows inside H II regions (Ochsendorf et al. 2014b,a; Ochsendorf & Tielens 2015). We follow the nomenclature proposed by Ochsendorf et al. (2014a), in which *dust wave* refers to the weak coupling case and *bow wave* to the strong coupling case. More complex, hybrid scenarios are also possible, such as that

studied by van Marle et al. (2011), where a hydrodynamic bow shock forms, but the larger dust grains that accompany the stellar wind pass right through the shocked gas shell, and form their own dust wave at a larger radius.

In Tarango Yong & Henney (2018, hereafter Paper I), we proposed a new two-dimensional classification scheme for bow shapes: the projected planitude–alatitude, or  $\Pi' - \Lambda'$ , diagram. Planitude measures the flatness of the bow’s apex, while alatitude measures the openness of the bow’s wings. Both are dimensionless ratios of lengths that can be estimated from observational images. We have analyzed the inclination-dependent tracks on the  $\Pi' - \Lambda'$  plane for simple geometric shapes (spheroids, paraboloids, hyperboloids) and for thin-shell hydrodynamic bow shock models (wilkinoid, cantoids, ancantoids). In this paper, we will do the same for simple models of radiation-driven dust waves (dragoids) and bow waves (trapoids).

The paper is organized as follows. In § 3 we do the same for simple models of a dusty radiation bow wave (dragoids), including the effects of gas–grain drag. In § 5 we investigate the effects on the planitude–alatitude plane of small-amplitude perturbations to the bow shape.

## 2 DIFFERENT TYPES OF BOW

In this section, we investigate the different types of bow interaction that will occur in different regions of parameter space. We will

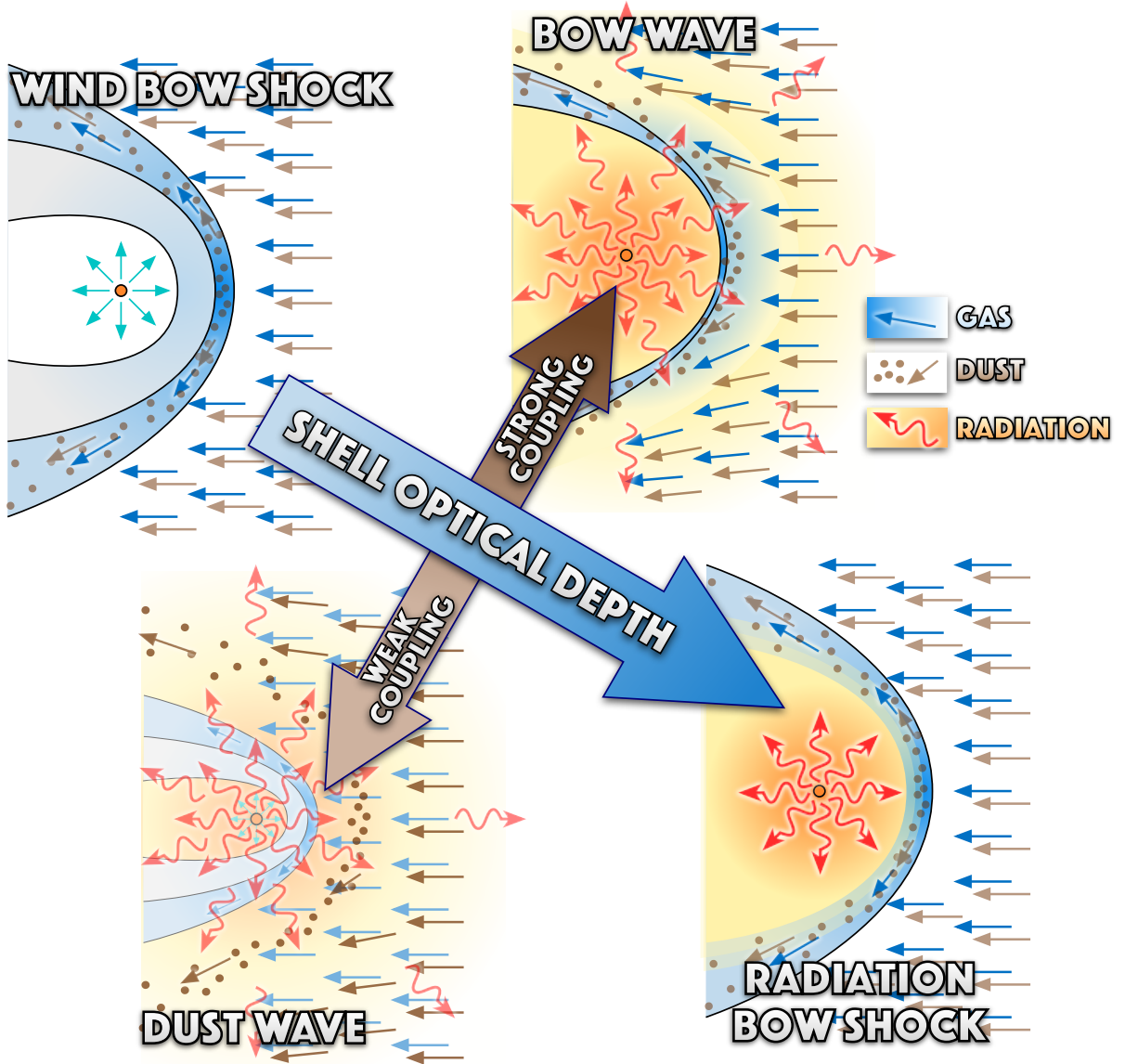


**Figure 1.** Bow shocks, bow waves, and dust waves

mainly treat the canonical case<sup>1</sup> of a bow around a star of bolometric luminosity,  $L$ , with a radiatively driven wind, which is immersed in an external stream of gas and dust with density,  $\rho$ , and velocity,  $v$ . The size and shape of the bow is determined by a generalized balance of pressure (or, equivalently, momentum) between internal and external sources. We assume that the stream is supersonic and super-alfvenic, so that the external pressure is dominated by the ram pressure:  $\rho v^2$ .

<sup>1</sup> Variant cases with differing arrangements of dust and radiation sources are treated in § 2.3.

### 2.1 Strong gas-grain coupling

We first consider the case where the dust grains and gas are perfectly coupled by collisions.<sup>2</sup> Although dust grains typically constitute only a small fraction  $Z_d \sim 0.01$  of the mass of the external stream, they nevertheless dominate the broad-band opacity at FUV, optical and

<sup>2</sup> Cases where this assumption does not hold are investigated below in § 2.2.



**Figure 2.** Bow regimes in parameter space ( $v, n$ ) of the external stream for main-sequence OB stars of different masses: (a)  $10 M_{\odot}$ , (b)  $20 M_{\odot}$ , (c)  $40 M_{\odot}$ . In all cases,  $\kappa = 600 \text{ cm}^2 \text{ g}^{-1}$  and efficient gas-grain coupling is assumed. Solid black lines of varying width show the bow size (star-apex separation,  $R_0$ ), while gray shading shows the radiation bow wave regime, with lower border  $\tau = \eta$  and upper border  $\tau = 1$ , where  $\tau = 2\kappa\rho R_0$  is the optical depth through the bow. For bows above the red solid line, the ionization front is trapped inside the bow. Blue lines delineate different cooling regimes. Above the thin blue line ( $d_{\text{cool}} = h_0$ ), the bow shock radiates efficiently, forming a thin shocked shell. Below the thick blue line ( $d_{\text{cool}} = R_0$ ), the bow shock is essentially non-radiative.

IR wavelengths if they are present.<sup>3</sup> The strong coupling assumption means that all the radiative forces applied to the dust grains are directly felt by the gas also.

The internal pressure is the sum of wind ram pressure and the effective radiation pressure that acts on the bow shell. The radiative momentum loss rate of the star is  $L/c$  and the wind momentum loss rate can be expressed as

$$\dot{M}V = \eta L/c, \quad (1)$$

where  $\eta$  is the momentum efficiency of the wind, which is typically  $< 1$  (Lamers & Cassinelli 1999). If the optical depth is very large, then all of the stellar radiative momentum, emitted with rate  $L/c$ , is trapped by the bow shell. In the single scattering limit,<sup>4</sup> and temporarily neglecting the wind, then pressure balance at the bow apex, a distance  $R_0$  along the symmetry axis from the star is given by

$$\frac{L}{4\pi c R_0^2} = \rho v^2, \quad (2)$$

which yields a fiducial bow shock radius in this optically thick limit

<sup>3</sup> At EUV wavelengths ( $\lambda < 912 \text{ \AA}$ ), gas opacity dominates if the hydrogen neutral fraction is larger than  $\approx 0.001$ , see discussion of ionization front trapping below.

<sup>4</sup> Although it may seem inconsistent to assume single scattering in the case of high optical depths, this is defensible for the following reasons. (1) The grain albedo is not that high (typically  $\sim 0.5$  at ultraviolet through optical wavelengths). (2) The scattered radiation field is more isotropic than the stellar field, leading to cancellation in the radiative flux. (3) Absorbed radiation is re-emitted at infrared wavelengths, where the dust opacity is very much lower.

as

$$R_* = \left( \frac{L}{4\pi c \rho v^2} \right)^{1/2}. \quad (3)$$

We now consider the opposite, optically thin limit. If the total opacity (gas plus dust) per total mass (gas plus dust) is  $\kappa$  (with units of  $\text{cm}^2 \text{ g}^{-1}$ ), then the radiative acceleration is

$$a_{\text{rad}} = \frac{\kappa L}{4\pi c R^2}. \quad (4)$$

Therefore, an incoming stream with initial velocity,  $v_{\infty}$ , can be brought to rest by radiation alone<sup>5</sup> at a distance  $R_0$  where

$$\int_{R_0}^{\infty} a_{\text{rad}} dr = \frac{1}{2} v_{\infty}^2, \quad (5)$$

yielding

$$R_0 = \frac{\kappa L}{2\pi c v_{\infty}^2}. \quad (6)$$

On the other hand, we can also argue as in the optically thick case above by approximating the bow shell as a surface, and balancing stellar radiation pressure against the ram pressure of the incoming stream. The important difference when the shell is not optically thick

<sup>5</sup> For simplicity, we here ignore the effects of gravity, which are important for low ratios of  $\kappa L/M$ , see § 2.1.1. We also ignore pressure gradients and shocks, which are important as the velocity approaches the sound speed,  $c_s$  (in § XX below, we show that the resultant corrections to  $R_0$  are of order  $c_s/v_{\infty}$ ).

is that only a fraction  $1 - e^{-\tau}$  of the radiative momentum is absorbed by the bow, so that equation (2) is replaced with

$$\frac{L(1 - e^{-\tau})}{4\pi c R_0^2} = \rho v^2. \quad (7)$$

In the optically thin limit,  $1 - e^{-\tau} \approx \tau$ , so these two descriptions can be seen to agree so long as

$$\tau = 2\kappa\rho R_0, \quad (8)$$

which we will assume to hold generally.

Then, defining a fiducial optical depth,

$$\tau_* = \rho\kappa R_*, \quad (9)$$

and adding in the stellar wind ram pressure<sup>6</sup> from equation (1), we find that the general bow radius can be written in terms of the fiducial radius as  $R_0 = xR_*$ , where  $x$  is the solution of

$$x^2 - (1 - e^{-2\tau_* x}) - \eta = 0. \quad (10)$$

Since this is a transcendental equation,  $x$  must be found numerically, but we can write explicit expressions for three limiting cases:

$$x \approx \begin{cases} \text{if } \tau_* \gg 1: & (1 + \eta)^{1/2} \\ \text{if } \tau_*^2 \ll 1: & \tau_* + (\tau_*^2 + \eta)^{1/2} \approx \begin{cases} \text{if } \tau_*^2 \gg \eta: & 2\tau_* \\ \text{if } \tau_*^2 \ll \eta: & \eta^{1/2} \end{cases} \end{cases} \quad (11)$$

The first case,  $x \approx (1 + \eta)^{1/2}$ , corresponds to a *radiation bow shock*; the second case,  $x \approx 2\tau_*$ , corresponds to a *radiation bow wave*; and the third case,  $x \approx \eta^{1/2}$ , corresponds to a *wind bow shock*. The two bow shock cases are similar in that the external stream is oblivious to the presence of the star until it suddenly hits the bow shock shell, differing only in whether it is radiation or wind that is providing the internal pressure. In the intermediate bow wave case, on the other hand, the external stream is gradually decelerated by absorption of photons as it approaches the bow.<sup>7</sup>

We now consider the application to bow shocks around main sequence OB stars, expressing stellar and ambient parameters in terms of typical values as follows:

$$\begin{aligned} \dot{M}_{-7} &= \dot{M}/(10^{-7} M_\odot \text{ yr}^{-1}) \\ V_3 &= V/(1000 \text{ km s}^{-1}) \\ L_4 &= L/(10^4 L_\odot) \\ v_{10} &= v_\infty/(10 \text{ km s}^{-1}) \\ n &= (\rho/\bar{m})/(1 \text{ cm}^{-3}) \\ \kappa_{600} &= \kappa/(600 \text{ cm}^2 \text{ g}^{-1}), \end{aligned}$$

where  $\bar{m}$  is the mean mass per hydrogen nucleon ( $\bar{m} \approx 1.3m_p \approx 2.17 \times 10^{-24} \text{ g}$  for solar abundances). Note that  $\kappa = 600 \text{ cm}^2 \text{ g}^{-1}$  corresponds to a cross section of  $\approx 10^{-21} \text{ cm}^2$  per hydrogen nucleon, which is typical for interstellar medium dust (Bertoldi & Draine 1996) at far ultraviolet wavelengths, where OB stars emit most of their radiation. In terms of these parameters, we can express the stellar wind momentum efficiency as

$$\eta = 0.495 \dot{M}_{-7} V_3 L_4^{-1} \quad (12)$$

<sup>6</sup> We implicitly assume that the interaction of the stellar wind with the external stream can always be treated in the continuum limit. This will be true if either the collisional mean free path or the ion Larmor radius is much smaller than  $R_0$ , which is almost always the case.

<sup>7</sup> A shock does still form in this case, but shocked material constitutes only a fraction of the total column density of the shell, see § 4.

and the fiducial radius and optical depth as

$$R_*/\text{pc} = 2.21 (L_4/n)^{1/2} v_{10}^{-1} \quad (13)$$

$$\tau_* = 0.0089 \kappa_{600} (L_4 n)^{1/2} v_{10}^{-1}. \quad (14)$$

In Figure 2, we show results for the bow size (apex distance,  $R_0$ ) as a function of the density,  $n$ , and relative velocity,  $v_\infty$ , of the external stream, with each panel corresponding to a particular star, with parameters as shown in Table 1. To facilitate comparison with previous work, we choose stellar parameters similar to those used in the hydrodynamical simulations of Meyer et al. (2014, 2016, 2017), based on stellar evolution tracks for stars of  $10 M_\odot$ ,  $20 M_\odot$  and  $40 M_\odot$  (Brott et al. 2011) and theoretical wind prescriptions (de Jager et al. 1988; Vink et al. 2000). Although the stellar parameters do evolve with time, they change relatively little during the main-sequence lifetime of several million years.<sup>8</sup> The three examples are an early B star ( $10 M_\odot$ ), a late O star ( $20 M_\odot$ ), and an early O star ( $40 M_\odot$ ), which cover the range of luminosities and wind strengths expected from bow-producing hot main sequence stars. The luminosity is a steep function of stellar mass ( $L \sim M^{2.5}$ ) and the wind mass-loss rate is a steep function of luminosity ( $\dot{M} \sim L^{2.2}$ ), which means that the wind momentum efficiency is also a steep function of mass ( $\eta \sim M^3$ ), approaching unity for early O stars, but falling to less than 1% for B stars.

It can be seen from Figure 2 that the onset of the radiation bow wave regime is very similar for the three main-sequence stars, occurring at  $n > 20$  to  $40 v_{10}^2$ . An important difference, however, is that for the  $40 M_\odot$  star, which has a powerful wind, the radiation bow wave regime only occurs for a very narrow range of densities, whereas for the  $10 M_\odot$  star, with a much weaker wind, the regime is much broader, extending to  $n < 10^4 v_{10}^2$ . Another difference is the size scale of the bows in this regime, which is  $R_0 = 0.001 \text{ pc}$  to  $0.003 \text{ pc}$  for the  $10 M_\odot$  star if  $v_\infty = 40 \text{ km s}^{-1}$ , but  $R_0 \approx 0.1 \text{ pc}$  for the  $40 M_\odot$  star, assuming the same inflow velocity.

Figure 3 shows results for a cool M-type super-giant star with stellar parameters inspired by Betelgeuse ( $\alpha$  Orionis), as listed in Table 1. Unlike the UV-dominated spectrum of the hot stars, this star emits predominantly in the near-infrared, where the dust extinction efficiency is lower, so we adopt a lower opacity of  $60 \text{ cm}^2 \text{ g}^{-1}$ . This has the effect of shifting the radiation bow wave regime to higher densities:  $n = 1000$  to  $30000 v_{10}^2$  in this case.

### 2.1.1 Effects of stellar gravity

In principle, gravitational attraction from the star, of mass  $M$ , will partially counteract the radiative acceleration. This can be accounted for by replacing  $L$  with an effective luminosity

$$L_{\text{eff}} = L(1 - \Gamma_E^{-1}), \quad (15)$$

<sup>8</sup> Note that we have recalculated the stellar wind terminal velocities, since the values given in the Meyer et al. papers are troublingly low. We have used the prescription  $V = 2.6V_{\text{esc}}$ , where  $V_{\text{esc}} = (2GM(1 - \Gamma_e)/R)^{1/2}$  is the photospheric escape velocity, which is appropriate for strong line-driven winds with  $T_{\text{eff}} > 21000 \text{ K}$  (Lamers et al. 1995). We find velocities of  $2500 \text{ km s}^{-1}$  to  $3300 \text{ km s}^{-1}$ , which are consistent with observations and theory (Vink et al. 1999) for O stars, but at least two times higher than those cited by Meyer et al. (2014). For main-sequence B stars, wind column densities are too low to reliably measure the terminal velocity from near ultraviolet P Cygni profiles (Prinja 1989), and so the values are theory-dependent (Krtička 2014) and hence more uncertain. A further complication is the existence of a subset of OB stars with anomalously weak winds (Puls et al. 2008), which in some cases is related to the presence of strong ( $\sim 1 \text{ kG}$ ) magnetic fields (Oskinova et al. 2011).

**Table 1.** Stellar parameters for example stars

	$M/M_{\odot}$	$L_4$	$\dot{M}_{-7}$	$V_3$	$\eta$	Sp. Type	$T_{\text{eff}}/\text{kK}$	$\lambda_{\text{eff}}/\mu\text{m}$	$S_{49}$	Figures
Main-sequence OB stars	10	0.63	0.0034	2.47	0.0066	B1.5 V	25.2	0.115	0.00013	2a, 6, 7
	20	5.45	0.492	2.66	0.1199	O9 V	33.9	0.086	0.16	2b
	40	22.2	5.1	3.31	0.4468	O5 V	42.5	0.068	1.41	2c
Blue supergiant star	33	30.2	20.2	0.93	0.3079	B0.7 Ia	23.5	0.123	0.016	4
Red supergiant star	20	15.6	100	0.015	0.0476	M1 Ia	3.6	0.805	0	3

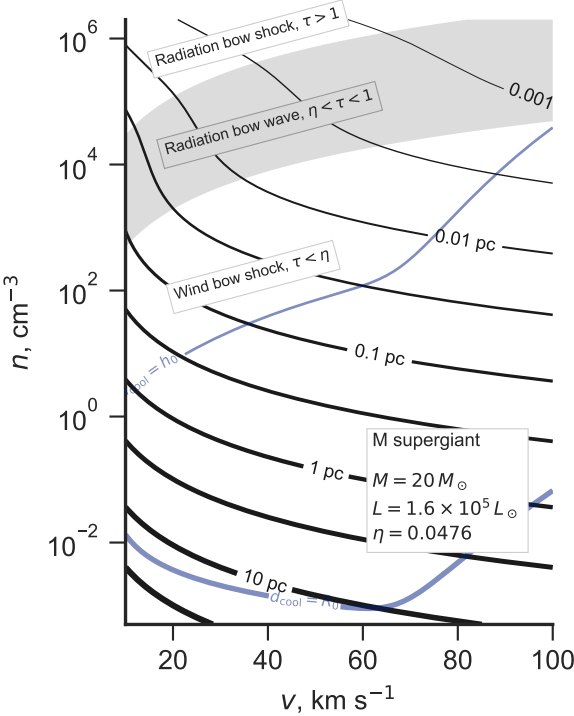


**Figure 3.** As Fig. 2, but for a cool M-type supergiant instead of hot main sequence stars. A smaller dust opacity is used,  $\kappa = 60 \text{ cm}^2 \text{ g}^{-1}$ , because of the reduced extinction efficiency at the optical/infrared wavelengths emitted by this star.

in which  $\Gamma_E$  is the Eddington factor:

$$\Gamma_E = \frac{\kappa L}{4\pi c GM} = 458.5 \frac{\kappa_{600} L_4}{M}, \quad (16)$$

where, in the last expression,  $M$  is measured in solar masses. For the stars in Table 1, we find  $\Gamma_E \approx 30$  to  $400$ , so gravity can be safely ignored. The only exception is when the optical depth of the bow is very large:  $\tau > \ln \Gamma_E \sim 5$ , in which case gravity may be important in the outer parts of the shell (see Rodríguez-Ramírez & Raga 2016).

### 2.1.2 Ionization state of the bow shell

In this section we calculate whether the star is capable of photoionizing the entire bow shock shell, or whether the ionization front will be trapped within it. The number of hydrogen recombinations<sup>9</sup> per

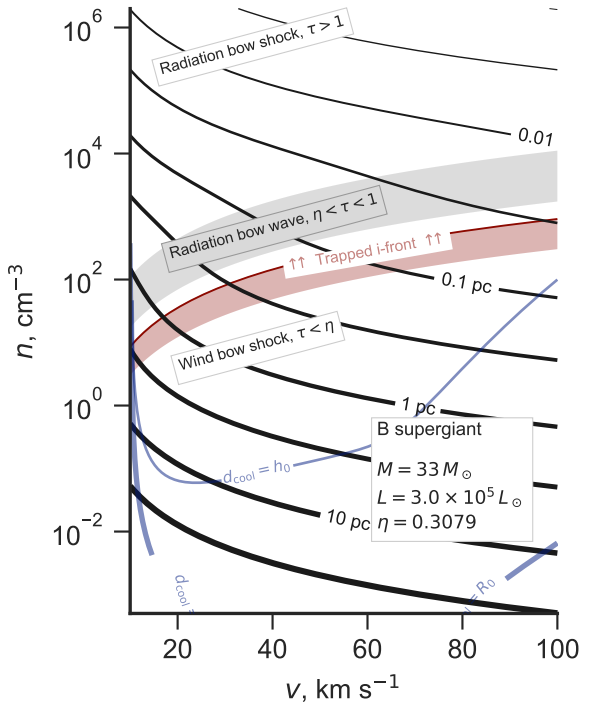


**Figure 4.** As Fig. 2, but for an evolved B-type supergiant instead of main sequence stars. This is similar to the early O MS star of Fig. 2c in many respects, except for the trapping of the ionization front, which occurs for much lower outer stream densities.

unit time per unit area in a fully ionized shell is

$$\mathcal{R} = \alpha_B n_{\text{sh}}^2 h_{\text{sh}}, \quad (17)$$

while the advective flux of hydrogen nuclei through the shock is

$$\mathcal{A} = nv, \quad (18)$$

and the flux of hydrogen-ionizing photons ( $h\nu > 13.6 \text{ eV}$ ) incident on the inner edge of the shell is

$$\mathcal{F} = \frac{S}{4\pi R_0^2}, \quad (19)$$

where  $S$  is the ionizing photon luminosity of the star. Any shell with  $\mathcal{R} + \mathcal{A} > \mathcal{F}$  cannot be entirely photoionized by the star, and so must have trapped the ionization front.

<sup>9</sup> The diffuse field is treated in the on-the-spot approximation, assuming all emitted Lyman continuum photons are immediately re-absorbed locally, so

the case B recombination co-efficient,  $\alpha_B = 2.6 \times 10^{-13} T_4^{-0.7} \text{ cm}^3 \text{ s}^{-1}$ , is used, where  $T_4 = T/10^4 \text{ K}$ .

## 6 Henney, Arthur, & Tarango Yong

The ratio of advective particle flux to ionizing flux is, from equations (3), (18), (19),

$$\frac{\mathcal{A}}{\mathcal{F}} = 5.86 \times 10^{-5} \frac{x^2 L_4}{v_{10} S_{49}}, \quad (20)$$

which is nearly always small. For clarity of exposition, we therefore ignore  $\mathcal{A}$  in the following discussion, although it is included in quantitative calculations. The column density of the shocked shell can be found, for example, from equations (10) and (12) of Wilkin (1996) in the limit  $v_\infty/V \rightarrow 0$  (Wilkin's parameter  $\alpha$ ) and  $\theta \rightarrow 0$ . This yields

$$n_{\text{sh}} h_{\text{sh}} = \frac{3}{4} n R_0. \quad (21)$$

Assuming strong cooling behind the shock,<sup>10</sup> the shell density is

$$n_{\text{sh}} = M_0^2 n \quad (22)$$

where  $M_0 = v_\infty/c_s$  is the isothermal Mach number of the external stream.<sup>11</sup> Putting these together with equations (3) and (9), one finds that  $\mathcal{R} > \mathcal{F}$  implies

$$x^3 \tau_* > \frac{4 S c_s \bar{m}^2 \kappa}{3 \alpha L}. \quad (23)$$

From equation (10), it can be seen that  $x$  depends on the external stream parameters,  $n, v_\infty$  only via  $\tau_*$ , and so equation (23) is a condition for  $\tau_*$ , which, by using equation (14), becomes a condition on  $n/v_{10}^2$ . In the radiation bow shock case,  $x = (1 + \eta)^{1/2}$ , and the condition can be written:

$$\frac{n}{v_{10}^2} > 2.65 \times 10^8 \frac{S_{49}^2 T_4^{3.4}}{L_4^3 (1 + \eta)^3}, \quad (24)$$

where

$$S_{49} = S/(10^{49} \text{ s}^{-1}).$$

Numerical values of  $S_{49}$  for our three example stars are given in Table 1, taken from Figure 4 of Sternberg et al. (2003). In the radiation bow wave case,  $x = 2\tau_*$ , and the condition can be written:

$$\frac{n}{v_{10}^2} > 5.36 \times 10^4 \frac{S_{49}^{1/2} T_4^{0.85}}{\kappa_{600}^{3/2} L_4^{3/2}}. \quad (25)$$

In the wind bow shock case, the result is the same as equation (24), but changing the factor  $(1 + \eta)^3$  to  $\eta^3$ . For the example hot stars in Table 1, and assuming  $\kappa_{600} = 1, T_4 = 0.8$ , the resulting density threshold is  $n > (1000 \text{ to } 5000) v_{10}^2$ , depending only weakly on the stellar parameters, which is shown by the red lines in Figure 2. For the  $10 M_\odot$  star, this is in the radiation bow wave regime, whereas for the higher mass stars it is in the radiation bow shock regime. When the external stream is denser than this, then the outer parts of the shocked shell may be neutral instead of ionized, giving rise to a cometary compact H II region (Mac Low et al. 1991; Arthur & Hoare 2006). This is only necessarily true, however, when the star is isolated. If the star is in a cluster environment, then the contribution of other nearby massive stars to the ionizing radiation field must be considered.

<sup>10</sup> This is shown to be justified in § 2.1.3.

<sup>11</sup> The sound speed depends on the temperature and hydrogen and helium ionization fractions,  $y$  and  $y_{\text{He}}$  as  $c_s^2 = (1 + y + z_{\text{He}} y_{\text{He}})(kT/\bar{m})$ , where  $z_{\text{He}}$  is the helium nucleon abundance by number relative to hydrogen and  $k = 1.3806503 \times 10^{-16} \text{ erg K}^{-1}$  is Boltzmann's constant. We assume  $y = 1$ ,  $y_{\text{He}} = 0.5$ ,  $z_{\text{He}} = 0.09$ , so that  $c_s = 11.4 T_4^{1/2} \text{ km s}^{-1}$ .

Quite different results are obtained for a B-type supergiant star (see Tab. 1 and Fig. 4), which has a similar bolometric luminosity and wind strength to the  $40 M_\odot$  main-sequence star, but a hundred times lower ionizing luminosity. This results in a far lower threshold for trapping the ionization front of  $n > 40 v_{10}^2$ . The advective flux,  $\mathcal{A}$ , is relatively stronger for this star than for the main-sequence stars, but even for  $v_{10} < 2$ , where the effect is strongest, the change is only of order the width of the dark red line in Figure 4.

In principle, when the ionization front trapping occurs in the bow wave regime, then the curves for  $R_0$  will be modified in the region above the red line because all of the ionizing radiation is trapped in the shell due to gas opacity, which is not included in equation (8). However, this only happens for our  $10 M_\odot$  star, which has a relatively soft spectrum. Table 1 gives the peak wavelength of the stellar spectrum for this star as  $\lambda_{\text{eff}} = 0.115 \mu\text{m}$ , which is significantly larger than the hydrogen ionization threshold at  $0.0912 \mu\text{m}$ , meaning that only a small fraction of the total stellar luminosity is in the EUV band and affected by the gas opacity. The effect on  $R_0$  is therefore small. For the higher mass stars,  $\lambda_{\text{eff}} < 0.0912 \mu\text{m}$ , so the majority of the luminosity is in the EUV band, but in these cases the ionization front trapping occurs well inside the radiation bow shock zone, where the dust optical depth is already sufficient to trap all of the radiative momentum.

### 2.1.3 Radiative cooling lengths

In this section, we calculate whether the radiative cooling is sufficiently rapid behind the bow shock to allow the formation of a thin, dense shell. Since cooling is least efficient at low densities, we will assume that the wind bow shock regime applies unless otherwise specified. We label quantities just outside the shock by the subscript “0”, quantities just inside the shock (after thermalization, but before any radiative cooling) by the subscript “1”, and quantities after the gas has cooled back to the photoionization equilibrium temperature by the subscript “2”. Assuming a ratio of specific heats,  $\gamma = 5/3$ , the relation between the pre-shock and immediate post-shock quantities is

$$\frac{n_1}{n_0} = \frac{4 M_0^2}{M_0^2 + 3} \quad (26)$$

$$\frac{T_1}{T_0} = \frac{1}{16} (5 M_0^2 - 1) (1 + 3/M_0^2) \quad (27)$$

$$\frac{v_1}{v_0} = \left( \frac{n_1}{n_0} \right)^{-1}, \quad (28)$$

where  $M_0 = v_0/c_s$ . The cooling length of the post-shock gas can be written as

$$d_{\text{cool}} = \frac{3 P_1 v_1}{2(\mathcal{L}_1 - \mathcal{G}_1)}, \quad (29)$$

where  $P_1$  is the thermal pressure and  $\mathcal{L}_1, \mathcal{G}_1$  are the volumetric radiative cooling and heating rates. For fully photoionized gas, we have  $P_1 \approx 2n_1 k T_1$ ,  $\mathcal{L}_1 = n_1^2 \Lambda(T_1)$ , and  $\mathcal{G}_1 = n_1^2 \Gamma(T_1)$ , where  $\Lambda(T)$  is the cooling coefficient, which is dominated by metal emission lines that are excited by electron collisions, and  $\Gamma(T)$  is the heating coefficient, which is dominated by hydrogen photo-electrons (Osterbrock & Ferland 2006). The cooling coefficient has a maximum around  $10^5 \text{ K}$ , and for typical ISM abundances can be approximated

as follows:

$$\Lambda_{\text{warm}} = 3.3 \times 10^{-24} T_4^{2.3} \text{ erg cm}^{-3} \text{ s}^{-1} \quad (30)$$

$$\Lambda_{\text{hot}} = 10^{-20} T_4^{-1} \text{ erg cm}^{-3} \text{ s}^{-1} \quad (31)$$

$$\Lambda = (\Lambda_{\text{warm}}^{-k} + \Lambda_{\text{hot}}^{-k})^{-1/k} \quad \text{with } k = 3, \quad (32)$$

which is valid in the range  $0.7 < T_4 < 1000$ . We approximate the heating coefficient as

$$\Gamma = 1.77 \times 10^{-24} T_4^{-1/2} \text{ erg cm}^{-3} \text{ s}^{-1}, \quad (33)$$

where the coefficient is chosen so as to give  $\Gamma = \Lambda$  at an equilibrium temperature of  $T_4 = 0.8$ .

In Figure 2 we show curves calculated from equations (26) to (33), corresponding to  $d_{\text{cool}} = R_0$  (thick blue line) and  $d_{\text{cool}} = h_0$  (thin blue line), where  $h_0$  is the shell thickness in the efficient cooling case. In this context,  $n_0 = n$  and  $n_2 = n_{\text{sh}}$ , so that  $h_0$  follows from equations (21) and (22) as

$$h_0 = \frac{3}{4} M_0^{-2} R_0. \quad (34)$$

The bends in the curves at  $v \approx 50 \text{ km s}^{-1}$  are due to the maximum in the cooling coefficient  $\Lambda(T)$  around  $10^5 \text{ K}$ . For bows with outer stream densities above the thin blue line, radiative cooling is so efficient that the bow shock can be considered isothermal, and so the shell is dense and thin (at least, in the apex region). It can be seen that the ionization front trapping always occurs at densities larger than this, which justifies the use of equation (22) in the previous section. For bows with outer stream densities below the thick blue line, cooling is unimportant and the bow shock can be considered non-radiative. In this case the shell is thicker than in the radiative case,  $h_{\text{sh}}/R_0 \approx 0.2$  to  $0.3$ .<sup>12</sup> For bows with outer stream densities between the two blue lines, cooling does occur, albeit inefficiently, so that the shell thickness is set by  $d_{\text{cool}}$  rather than  $h_0$ .

## 2.2 Imperfect coupling between gas and dust

If the radiation field is sufficiently strong, then the collisional coupling between grains and gas will break down. In this section, we calculate the regions of star+stream parameter space where this might occur, leading to a separation of the bow into an outer dust wave and an inner, dust-free bow shock.

The drag force on a charged dust grain moving at a relative speed  $w$  through a plasma has contributions from both direct collisions and from electrostatic Coulomb interactions with ions and electrons. We use the expressions in Draine & Salpeter (1979), equations (4)–(6), summing over protons, electrons, and helium ions.<sup>13</sup> Results are shown in Figure 5 for different values of the dimensionless grain potential:  $\phi = e^2 Z_d / a k T$ , which is the electrostatic potential energy of a unit charge at the surface of a grain of charge  $Z_d$  and radius  $a$ , in units of the characteristic thermal energy of a gas particle. The drag force  $f_{\text{drag}}$  is put in dimensionless units by dividing by a characteristic force:

$$f_* = 2n k T \cdot \pi a^2, \quad (35)$$

<sup>12</sup> An approximate value can be found from equation (21) by substituting  $n = n_0$  and  $n_{\text{sh}} \approx n_1$ , then using equation (26). Consideration of the slight increase in density between the shock and the contact discontinuity reduces this value by 5–10%.

<sup>13</sup> Helium is assumed to be 50% neutral and 50% singly ionized, leading to only a small contribution to the drag force. For much hotter stars, such as the central stars of planetary nebulae, helium may be doubly ionized, which leads to a more significant drag contribution, especially around  $w \approx 5 \text{ km s}^{-1}$ .

which is approximately<sup>14</sup> the ionized gas pressure multiplied by the grain geometric cross section.

For grains with low electric charge,  $\phi^2 \ll 1$ , the drag force is dominated by direct collisions of protons with the grain (Epstein drag). This is illustrated by the  $\phi = 0.25$  case (blue line) in Figure 5. In the subsonic regime,  $f_{\text{drag}}$  increases linearly with the relative slip speed,  $w$ , reaching  $f_{\text{drag}} \approx f_*$  at  $w = c_s \approx 10 \text{ km s}^{-1}$ , then transitions to quadratic increase,  $f_{\text{drag}} \approx w^2 f_*/c_s^2$ , in the supersonic regime. As  $|\phi|$  increases, long-range electrostatic interactions with protons within the Debye radius (Coulomb drag) become increasingly important at subsonic relative velocities, as shown in Figure 5 by the orange ( $\phi = 1$ ), green ( $\phi = 4$ ), and red ( $\phi = 16$ ) lines. However, the Coulomb drag has a peak when  $w$  is equal to the thermal speed of the colliders, which is  $\approx 10 \text{ km s}^{-1}$  for protons, giving a maximum strength of

$$f_{\text{max}} = 0.5 (\ln \Lambda) \phi^2 f_* \approx 10 \phi^2 f_*, \quad (36)$$

where  $\Lambda$  is the plasma parameter (number of particles within a Debye volume), such that  $\ln \Lambda = 23.267 + 1.5 \ln T_4 - 0.5 \ln n$ . At highly super-thermal speeds, the Coulomb drag falls asymptotically as  $f_{\text{drag}} \propto 1/w^2$ . The thermal speed of electrons is higher by a factor of  $(m_p/m_e)^{1/2}$ , so that the electron Coulomb drag has a peak of similar strength, but at  $w \approx 430 \text{ km s}^{-1}$ .

## 2.3 The case of inside-out bows

So far, we have considered the case where the inner source dominates the radiation, while dust is present only in the outer stream, which applies to hot stars interacting with the ISM. However, in the case of cool stars, the inner wind will also be dusty. Examples are the red supergiant (RSG) phase of high-mass evolution, or the asymptotic giant branch (AGB) stage of low/intermediate-mass evolution. In both these cases, it is still the inner source that provides the radiation field. However, not all winds are radiatively driven and in those cases it is conceivable that it is the outer source that dominates the radiation field. An example is the case of photoevaporating protoplanetary disks (proplyds) in the Orion Nebula and other H II regions (O'Dell & Wen 1994). In the proplyds, the inner wind is a thermally driven photoevaporation flow (Henney & Arthur 1998; Henney & O'Dell 1999), while the outer stream is the stellar wind from an O star (García-Arredondo et al. 2001).

## 3 SHAPE AND STRUCTURE OF DUST WAVES

As an alternative to hydrodynamic or magnetohydrodynamic bow shocks, it is possible that some observed emission arcs may be bow waves due to the action of radiation pressure on dust grains.

A dust grain of geometrical cross-section  $\sigma_d$  situated a distance  $R$  from a point source of radiation with luminosity  $L$  will experience a repulsive, radially directed radiative force (e.g., Spitzer 1978)

$$f_{\text{rad}} = \frac{\sigma_d Q_p L}{4\pi R^2 c} e^{-\tau} \quad (37)$$

where  $Q_p$  is the frequency-averaged<sup>15</sup> radiation pressure efficiency<sup>16</sup>

<sup>14</sup> Exact in the case of a fully ionized, pure hydrogen plasma. For typical ISM abundances, the contribution to the gas pressure of helium and its corresponding electrons gives a correction of order 5%.

<sup>15</sup> Frequency averages of any quantity  $x$  should be understood as weighted by the attenuated source spectrum:  $\langle x \rangle_\nu = (L e^{-\tau})^{-1} \int_0^\infty x(\nu) L_\nu e^{-\tau_\nu} d\nu$ .

<sup>16</sup> For absorption efficiency  $Q_{\text{abs}}$ , scattering efficiency  $Q_{\text{scat}}$ , and asymmetry

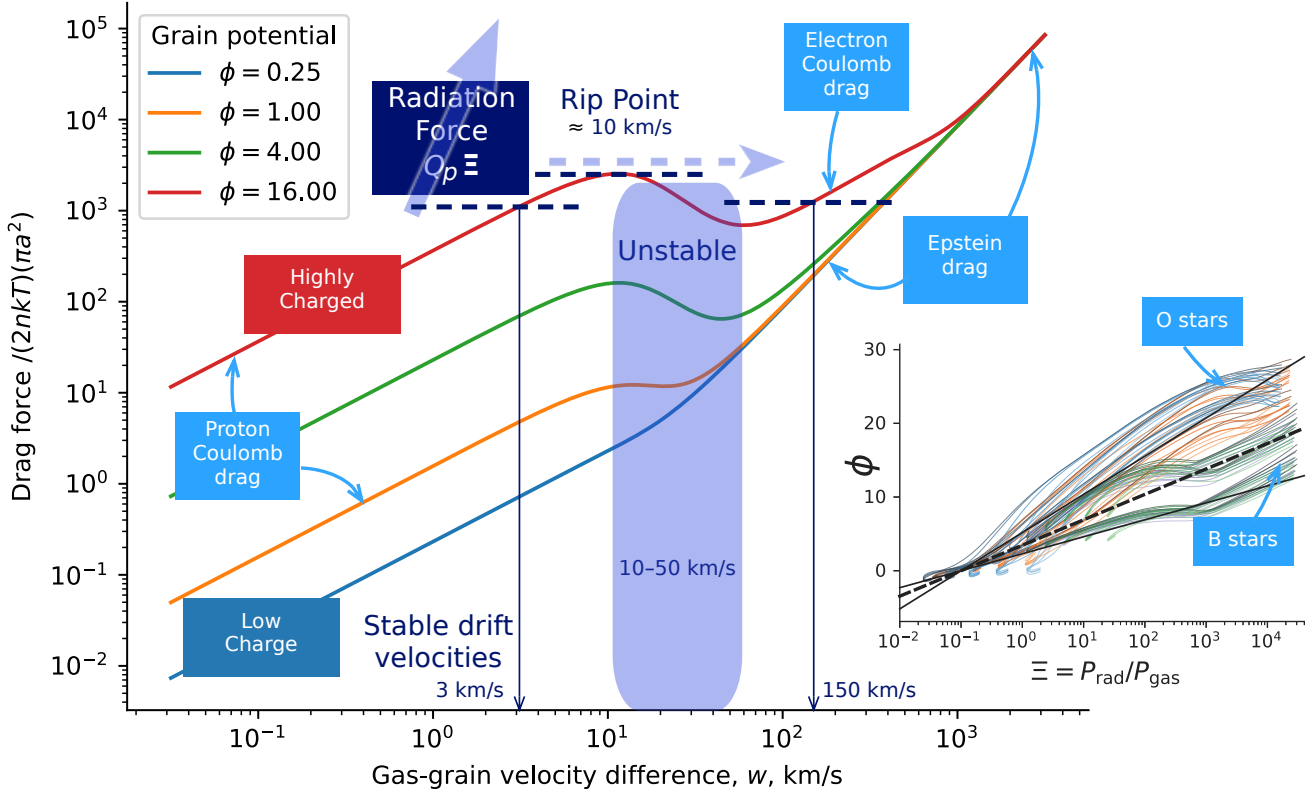


**Figure 5.** Dimensionless drag force,  $f_{\text{drag}}/f_e$ , as a function of gas–grain slip velocity,  $w$ , for different values of the grain potential in thermal units,  $\phi$ . Contributions from proton and electron Coulomb (electrostatic) drag, as well as Epstein (solid-body) drag are indicated. Examples of subsonic and highly supersonic stable drift velocities are shown (thin dark blue arrows), where the drag force is in equilibrium with the radiation force (thick dark blue dashed lines), while blue shading indicates the unstable, mildly supersonic velocity regime, where no stable drift equilibrium exists. Inset graph shows  $\phi$  as a function of the radiation parameter,  $\Xi = P_{\text{rad}}/P_{\text{gas}}$  on a log–linear scale for a collection of Cloudy models (see Appendix A).

of the grain,  $c$  is the speed of light, and  $\tau$  is the frequency-averaged optical depth between the source and the grain. For simplicity, we will consider only the optically thin case,  $\tau \rightarrow 0$ .

### 3.1 Gas-free dust wave

If  $f_{\text{rad}}$  is the only force experienced by the grain, then it will move on a *ballistic* trajectory, determined by its initial speed at large distance,  $v_\infty$ , and its impact parameter,  $b$ . For  $b = 0$ , the grain radially approaches the source with initial radial velocity  $-v_\infty$ , which is decelerated to zero at the distance of closest approach,  $R_0$ , given by energy conservation:

$$R_0 = \frac{\sigma_d Q_p L}{2\pi c m_d v_\infty^2}, \quad (38)$$

where  $m_d$  is the grain mass. The grain then turns round and recedes from the source along the same radius, reaching a velocity of  $+v_\infty$

parameter (mean scattering cosine)  $g$ , we have  $Q_p = Q_{\text{abs}} + (1-g)Q_{\text{scat}}$  (e.g., § 4.5 of Bohren & Huffman 1983).

at large distance. For  $b > 0$ , the trajectory,  $R_d(\theta; b)$ , is found<sup>17</sup> to be hyperbolic, characterized by an eccentricity,  $\varepsilon = (1 + 4b^2/R_0^2)^{1/2}$ , and polar angle of closest approach,  $\theta_m = \cos^{-1} \varepsilon^{-1}$ . The trajectory is symmetrical about  $\theta_m$  and can be written as

$$\frac{R_d(\theta; b)}{R_0} = \frac{\frac{1}{2}(\varepsilon^2 - 1)}{\varepsilon \cos(\theta - \theta_m) - 1}, \quad (39)$$

with a total deflection angle of  $2\theta_m$ , which is equal to  $90^\circ$  when  $b = 0.5R_0$ .

#### 3.1.1 Parallel dust stream

If the incoming dust grains initially travel along parallel trajectories with varying  $b$ , but the same  $v_\infty$ , then deflection by the radiative force will form a bow wave around the radiation source, as shown

<sup>17</sup> The problem is formally identical to that of Rutherford scattering, or (modulo a change of sign) planetary orbits. The method of solution (via introduction of a centrifugal potential term and reduction to a 1-dimensional problem) can be found in any classical mechanics text (e.g., Landau & Lifshitz 1976, § 14).

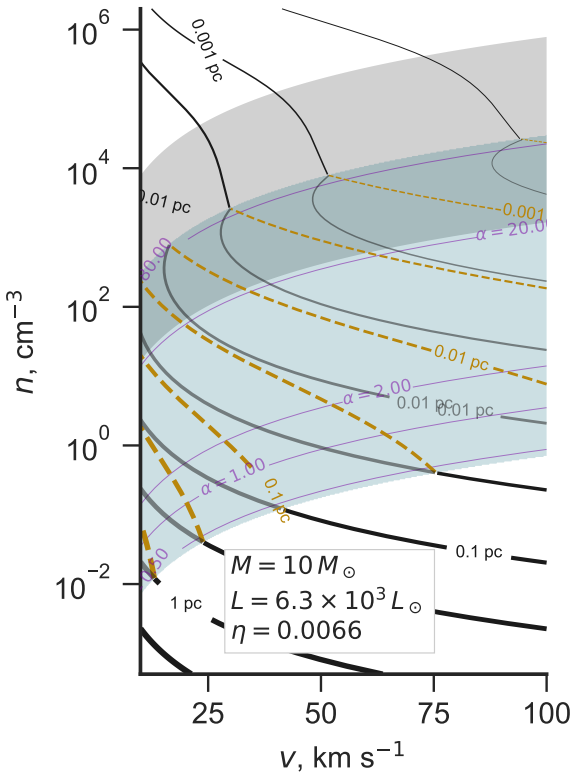


**Figure 6.** As Fig. 2(a), but accounting for gas-grain decoupling with constant efficiency  $\xi = 0.07$ .

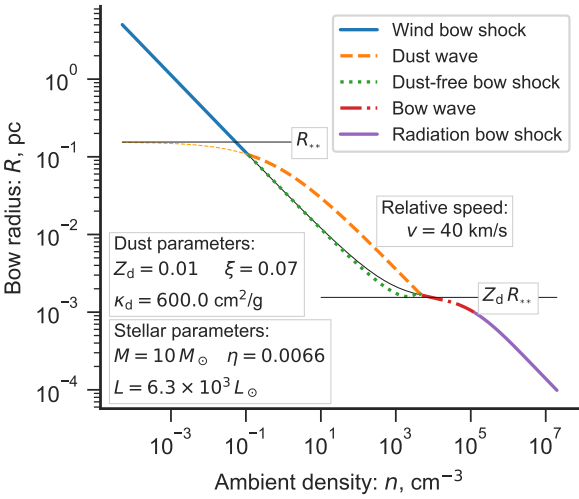


**Figure 7.** Vertical cut through Fig. 6, showing bow radius and different regimes for a fixed inflow velocity of  $40 \text{ km s}^{-1}$ .

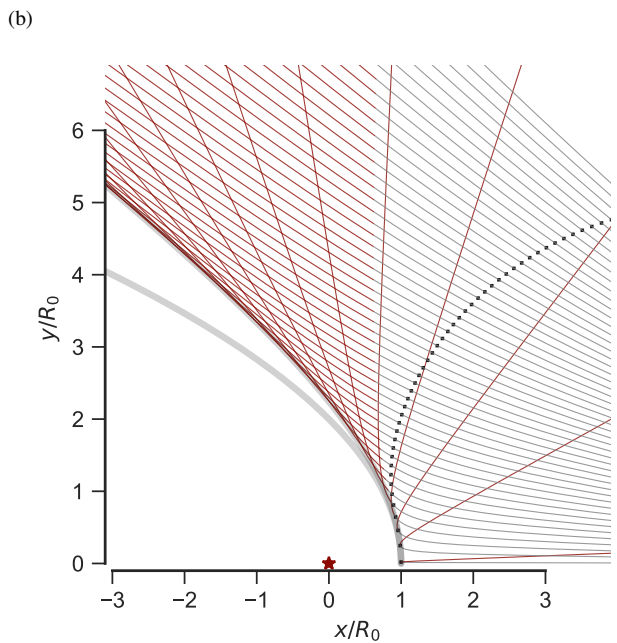
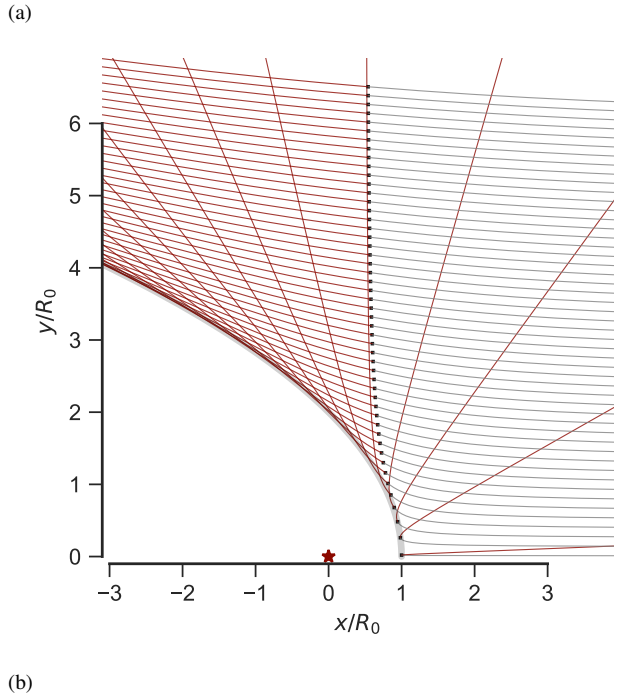


**Figure 8.** Dust grain trajectories under influence of a repulsive central  $r^{-2}$  radiative force. (a) A parallel stream of dust grains approach from the right at a uniform velocity and with a variety of impact parameters (initial  $y$ -coordinate). The central source is marked by a red star at the origin, and its radiative force deflects the trajectories into a hyperbolic shape, each of which reaches a minimum radius marked by a small black square. The incoming hyperbolic trajectories are traced in gray and the outgoing trajectories are traced in red. The locus of closest approach of the outgoing trajectories is parabolic in shape (traced by the thick, light gray line) and this constitutes the inner edge of the bow wave. (b) The same but for a divergent stream of dust grains that originates from a source on the  $x$  axis at a distance  $D = 10R_0$  from the origin. In this case, the inner edge of the bow wave is hyperbolic and the parallel stream result is also shown for comparison.

in Figure 8. However, the inner edge of the bow wave,  $R_{\text{in}}(\theta)$  is not given by the closest approach along individual trajectories,  $R_d(\theta_m; b)$ , but instead must be found by minimizing  $R_d(\theta; b)$  over all  $b$  for each value of  $\theta$ , which yields

$$\frac{R_{\text{in}}(\theta)}{R_0} = \frac{2}{1 + \cos \theta}. \quad (40)$$

This is the polar form of the equation for the confocal parabola, which we have already discussed in detail in Paper I's § 4 and Appendix C. Its planitude and alatitude are  $\Gamma = \Lambda = 2$  and these are unchanged under projection at any inclination.

### 3.1.2 Divergent dust stream

If the dust grains are assumed to originate from a second point source, located at a distance  $D$  from the radiation source, then the incoming stream will be divergent instead of plane parallel. The individual streamlines are not affected by this change and are still described by equation (39), except that the trajectory axes for  $b > 0$  are no longer aligned with the global symmetry axis, so we must make the substitution  $\theta \rightarrow \theta + \theta_1(b)$ , where  $\sin \theta_1 = b/D$  (see Fig. 3 of Paper I). We parametrize the degree of divergence as  $\mu = R_0/D$  and, as before,  $R_d(\theta + \theta_1(b, \mu); b)$  is minimized over all trajectories to find the shape of the bow wave's inner edge. This time, the result is a confocal hyperbola:

$$\frac{R_{\text{in}}(\theta; \mu)}{R_0} = \frac{1 + \varepsilon_\mu}{1 + \varepsilon_\mu \cos \theta}, \quad (41)$$

where the eccentricity is (to first order in  $\mu$ )  $\varepsilon_\mu = (1 - 2\mu)^{-1}$ . An example is shown in Figure 8 for  $\mu = 0.1$ . Unsurprisingly, the resulting bow shape is more open than in the parallel stream case, increasingly so with increasing  $\mu$ . The planitude and alatitude are both equal:  $\Pi = \Lambda = 1 + \varepsilon_\mu$ .

## 3.2 Bow wave with gas drag

More realistically, a grain will also be subject to a drag force,  $f_{\text{drag}}$ , due to its relative motion with respect to gas or plasma particles. If the gas density, velocity, and sound speed are  $\rho_{\text{gas}}$ ,  $v_{\text{gas}}$ , and  $c_{s,\text{gas}}$ , then a grain with velocity  $v_d$  will experience a drag force that is directed opposite to the relative velocity,  $w = v_d - v_{\text{gas}}$ . In the supersonic limit,  $w \equiv |w| \gg c_{s,\text{gas}}$ , the magnitude of the force is

$$|f_{\text{drag}}| \approx Q_{\text{drag}} \sigma_d \rho_{\text{gas}} w^2, \quad (42)$$

where  $Q_{\text{drag}}$  is an efficiency factor (which may be smaller or greater than unity) that accounts for details such as sticking probability and the boost in cross section due to the Coulomb force when a charged grain interacts with an ionized plasma (Draine & Salpeter 1979). We neglect the back reaction of the dust on the gas motion and assume a uniform background gas flow that is perfectly coupled to the incoming dust stream at large radii. So, for the parallel stream case, we have  $v_{\text{gas}} = -v_\infty \hat{x}$  everywhere.

Considering the incoming flow on the symmetry axis, at each radius there is an asymptotic gas-grain drift speed,  $w_{\text{drift}}$ , for which the radiative and drag forces exactly cancel,  $f_{\text{drag}} = -f_{\text{rad}}$ , yielding

$$w_{\text{drift}} = \left( \frac{Q_p L}{4\pi c Q_{\text{drag}} \rho_{\text{gas}} R^2} \right)^{1/2}. \quad (43)$$

Any deviation of  $w$  from  $w_{\text{drift}}$  produces unbalanced forces that tend to restore  $w \rightarrow w_{\text{drift}}$ , although the grain inertia means that this will not happen instantaneously, so that if  $w_{\text{drift}}$  varies rapidly

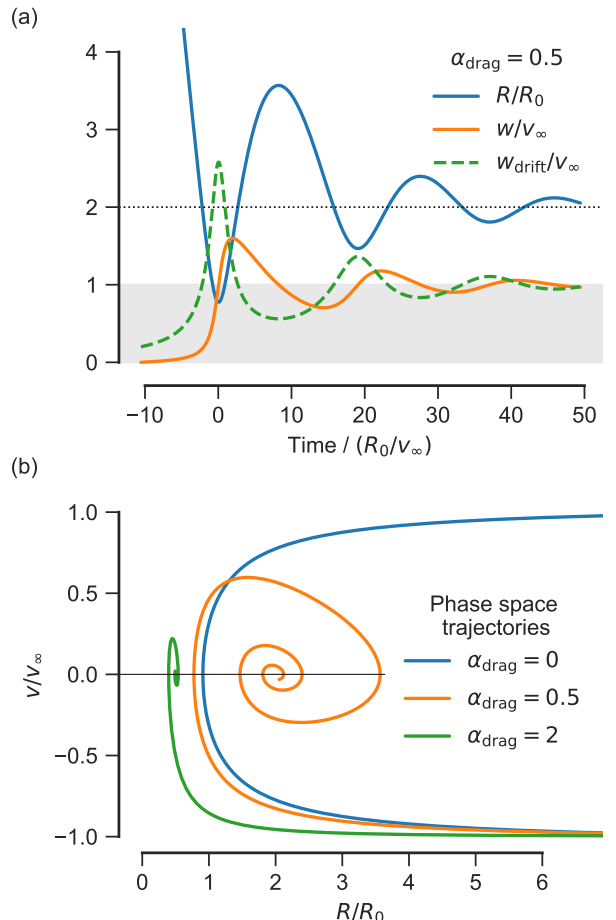


**Figure 9.** Dust-gas coupling for an on-axis (purely radial) trajectory. (a) Grain radial position,  $R/R_0$ , gas-grain velocity difference,  $w/v_\infty$ , and local asymptotic drift velocity,  $w_{\text{drift}}/v_\infty$ , versus time for  $\alpha_{\text{drag}} = 0.5$ . The behavior is typical of the dynamics of a damped harmonic oscillator. (b) Phase space (position, velocity) trajectories for  $\alpha_{\text{drag}} = 0$ , 0.5, and 2. All trajectories begin in the lower right corner and evolve in a clockwise direction. For  $\alpha_{\text{drag}} > 0$ , the grain spirals in on the point  $(x, u) = (\alpha_{\text{drag}}^{-1}, 0)$ .

along a streamline, then changes in  $w$  will lag behind. We define a dimensionless coupling coefficient,  $\alpha_{\text{drag}}$ , to be the speed of the incoming stream in units of the drift velocity at the radiative turn-around radius:

$$\alpha_{\text{drag}} \equiv \frac{v_\infty}{w_{\text{drift}}(R_0)} = \left( Q_{\text{drag}} \frac{R_0/a_{\text{ad}}}{\rho_d/\rho_{\text{gas}}} \right)^{1/2}, \quad (44)$$

where we have used equation (38) and suppressed a grain-shape dependent geometric factor of order unity. If  $\alpha_{\text{drag}} \ll 1$ , then  $w_{\text{drift}} \gg v_\infty$  out to several times the turn-around radius, so the radiation field has no difficulty in effectively decoupling the grain from the gas and producing the velocity difference that is required to turn the grain around and expel it towards the direction whence it came ( $w = 2v_\infty$ ). However, for non-zero  $\alpha_{\text{drag}}$  the  $R^{-1}$  dependence of  $w_{\text{drift}}$  (eq. (43)) means that the grain will *re-couple* to the inflowing gas stream around a radius  $\approx R_0/\alpha_{\text{drag}}$  and be swept back in again for another approach to the source. A further effect of increasing  $\alpha_{\text{drag}}$  is that the grain penetrates closer to the star on its initial approach, thanks to the tail wind provided by the gas flow. Both

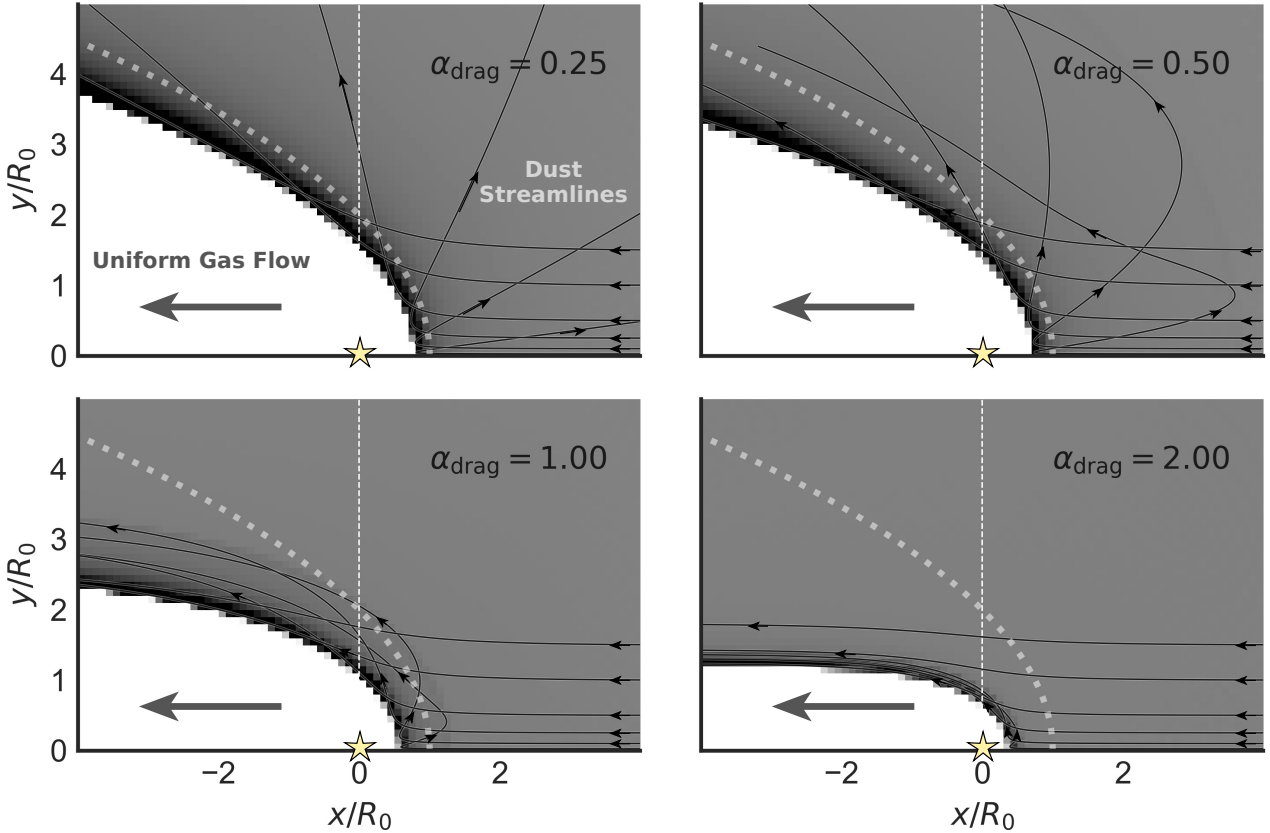


**Figure 10.** Dust grain trajectories under influence of gas drag in addition to a repulsive central radiative force. The dust streamlines are shown as black lines with arrows and the dust density as a linear gray scale, with maximum (black) of twice the ambient dust density. Results are shown for four values of the drag parameter (see text):  $\alpha_{\text{drag}} = 0.25, 0.5, 1.0$ , and  $2.0$ . The shape of the bow wave for the drag-free case (Fig. 8) is shown by the thick dotted line. Faint patterns visible in the density away from the bow wave are numerical aliasing artefacts caused by sparse sampling of the streamlines in the low density regions.

these behaviors are illustrated in Figure 9, where the inertial lag of  $w$  behind  $w_{\text{drift}}$  means that the phase space trajectory (panel b) is a spiral, which converges on the stagnation point  $(R, v) = (R_0/\alpha_{\text{drag}}, 0)$ . The cases  $\alpha_{\text{drag}} = 0.5$  and  $\alpha_{\text{drag}} = 2$  are shown, and it can be seen that with larger  $\alpha_{\text{drag}}$  the oscillations about the stagnation radius are significantly damped.

However, this description only applies to grains with impact parameter,  $b$ , that is exactly zero. Even a very small finite  $b$  means that  $f_{\text{rad}}$  has a component perpendicular to the axis, which pushes the grain to the side and means that, after re-coupling, its second approach is at a much larger impact parameter than its first, so it is dragged around the wings of the bow wave before it can bounce in and out more than twice. This is illustrated in Figure 10, which shows grain trajectories and the resulting dust density structure, calculated from numerical integration of equations (37) and (42) in 2-D cylindrical coordinates. Results are shown for a range of coupling parameters,  $\alpha_{\text{drag}}$ . The  $\alpha_{\text{drag}} = 0.25$  case appears qualitatively similar to the no-drag case shown in Figure 8a, except that the inner edge of the bow wave has been shifted to a smaller radius. Recoupling of the outgoing streamlines to the gas flow does occur eventually, but on length scales larger than shown in the figure. The  $\alpha_{\text{drag}} = 0.5$  case shows the oscillating trajectories discussed above for those grains that come in with a small initial impact parameter. In the  $\alpha_{\text{drag}} = 1.0$  case, the oscillating trajectories are more confined, forming a thick

shell around  $R_0$ . In the  $\alpha_{\text{drag}} = 2.0$  case, the shell is much thinner and concentrated at the inner rim. As  $\alpha_{\text{drag}}$  increases, the oscillations are damped further so that the stagnation radius  $R_0/\alpha_{\text{drag}}$  becomes a good approximation to the apex radius of the density wave. All the cases illustrated are for a parallel incident stream, but a divergent stream gives qualitatively similar behavior, as shown in Appendix B. We propose the term *dragoid* for the 3-dimensional shapes of the bow waves, found by rotating results such as Figure 10 about the symmetry axis.

### 3.3 Bow wave with magnetic field

First consider the limit of very small gyro-radius, which is the case when the Lorentz force is much larger than other forces acting on the grain. The grains will then follow tightly wound helical paths around the magnetic field lines, which can be decomposed into a circular motion of radius  $r_L$  plus the motion if the *guiding center* along the field line. The motion of the guiding center is explicitly followed by accounting for the components parallel to the field lines of the radiative and drag forces, whereas forces perpendicular to the field lines, which would only effect the circular motion are ignored in the first instance (but see § XXX below).

### 3.3.1 Resolved Larmor radius

## 3.4 Applicability of the bow wave models

The apex turn-around radius,  $R_0$ , of the bow wave depends on the grain properties via the combination  $\sigma_d Q_p / m_d$ . For grains of size  $a_d$  and internal density  $\rho_d$ , we have  $\sigma_d / m_d \approx (a_d \rho_d)^{-1}$ . For radiation with wavelength smaller than the grain size,  $\lambda < a_d$ , the efficiency is  $Q_p \sim 1$ , whereas for  $\lambda > a_d$  it is  $Q_p \sim a_d / \lambda$ . Therefore, we would expect  $R_0$  to be almost independent of grain size for small grains, but to vary as  $R_0 \propto a_d^{-1}$  for large grains, where small/large is relative to the peak wavelength of the radiation source. In principle, a polydisperse population of grains could produce a blurring of the observed bow wave, but only if large grains contribute significantly to the dust emission.

Variation of  $\alpha_{\text{drag}}$  with grain size, charged grains.

Lorentz force, Larmor radius

Back-reaction on gas,  $\alpha_{\text{drag}} \rightarrow \infty$ , recovery of drag-free result for  $R_0$  but with increased effective grain mass.

## 3.5 Apparent shapes of projected dragoids

## 4 SHAPE AND STRUCTURE OF BOW WAVES

## 5 PERTURBED BOWS

The bow shock models that we have considered so far have been steady-state: although material is moving throughout the bow, the pattern of its structure does not vary with time. In this section, we consider small, time-varying perturbations to such a steady-state structure. These may be due to periodic variations in the momentum-loss rate of one of the winds, or due to dynamical instabilities in the shocked shell.

We consider fractional perturbations  $\Delta(\theta, t)$  of a base shape  $R(\theta)$ , such that  $R(\theta) \rightarrow [1 + \Delta(\theta, t)]R(\theta)$ . For simplicity,  $\Delta(\theta, t)$  is a standing wave of constant amplitude  $A$ , which is periodic in  $\theta$ , with wave number  $N$ . In cylindrical symmetry  $\Delta(\theta, t)$  must be even in  $\theta$ , so can be expressed as

$$\Delta(\theta, t) = A \cos(N\theta) \cos(2\pi\varphi). \quad (45)$$

For waves with period  $P$ , the fractional phase  $\varphi$  will vary with time  $t$  as

$$\varphi(t) = (\varphi_0 + t/P) \bmod 1.0, \quad (46)$$

where  $\varphi_0$  is an arbitrary reference phase.

Example oscillations with wave numbers  $N = 1.0, 2.0$ , and  $5.0$  superimposed on a wilkinoid base shape are shown in Figure 19. There are  $N$  nodes of the oscillation between  $\theta = [0, \pi]$ , always with an antinode at the apex ( $\theta = 0$ ), as required by symmetry. So, with  $N = 1.0$  there is a node (fixed point) in the near wing at  $\theta = \pi/2$ , but an antinode in the far wing at  $\theta = \pi$ , which is in antiphase with the oscillation of the apex, giving rise to a large-scale “breathing” mode of oscillation. With  $N = 2.0$ , there are nodes at  $\theta = \pi/4$  and  $3\pi/4$ , while the antiphase antinode has moved to the near wing at  $\theta = \pi/2$ . There is still an antinode in the far wing at  $\theta = \pi$  but it is now in phase with the apex, giving rise to a “curling-up/straightening-out” mode of oscillation. With  $N = 5.0$ , there are many more nodes and antinodes, giving a “ringing” mode of oscillation. Note that all our examples have  $A \propto 1/N$  in order to keep the local curvature

relatively low. If the product  $AN$  is not small compared to unity, then the local curvature can be so extreme as to reverse the concave shape of the base bow shape, producing locally convex regions.

If the bow shape is viewed at different inclinations, then the effect of the oscillations on the projected shape will vary. In particular, the apex-to-wing interval in body-frame angle changes from  $\theta = [0, \pi/2]$  at  $i = 0$  to  $\theta = [\theta_0, \theta_{90}]$  for general  $i$ , see equations (18) and (21) of Paper I. The difference  $\theta_{90} - \theta_0$  is always a declining function of  $|i|$ , so the oscillations of the tangent line become increasingly stretched out as the inclination increases. This effect can be seen in Figure 20, which shows an example of the variation in projected perturbed shape with inclination angle for 3 different phases, this time for an ancantoid base shape and the  $N = 2.0$  perturbation shown in Figure 19b. The most marked changes with phase are seen for low inclinations, whereas the changes are smaller, although still noticeable, for  $|i| \geq 45^\circ$ . If  $AN$  exceeds about 0.5, then the local curvature of the perturbations is so extreme that multiple tangent lines exist at intermediate inclinations, which produces the appearance of additional incomplete bright arcs inside the main arc of the bow.

## 6 CASE STUDIES

Carina mid-infrared bow shocks (Sexton et al. 2015) are in a high density environment,  $1000 \text{ cm}^{-3}$ , so they may be bow waves. There seems to be spectral types for most of them: B0 (but supergiant) to O7. Sizes are 3 to 12 arcsec, which at Carina (2.3 kpc) is 0.033 pc to 0.134 pc.

Amazingly, the size/density combination gives regions that overlap with the dust wave region for both the  $20 M_\odot$  and  $40 M_\odot$  case. And implying velocities of  $30 \text{ km s}^{-1}$  to  $50 \text{ km s}^{-1}$ . This is more believable than the  $10 \text{ km s}^{-1}$  that they quote, since that would not give a shock at all. This would imply  $\tau > \eta \approx 0.1$ , so the bow luminosity should be 10% of the star luminosity, so getting on for  $10^4 L_\odot$ .

## 7 SUMMARY AND DISCUSSION

How different regions of the  $\Pi-\Lambda$  plane are populated. Bottom-right quadrant hard to get to (except for standing wave oscillations), but may be due to finite shell thickness, which (for low Mach number) will be more apparent in the wings, which might decrease  $\Lambda$  more than  $\Pi$ . Fact that thin-shell solutions should trace the contact discontinuity, but in some cases it may be only the inner or the outer shell that is visible.

Justification for standing waves: Fig. 3 of Meyer et al. (2016) shows a time sequence of thin-shell instability, which looks a bit like a standing wave. But much larger amplitude than we are considering.

Deviations from axisymmetry as an alternative to oscillations.

## REFERENCES

- Arthur S. J., Hoare M. G., 2006, ApJS, 165, 283
- Bertoldi F., Draine B. T., 1996, ApJ, 458, 222
- Bohren C. F., Huffman D., 1983, Absorption and scattering of light by small particles. Wiley-VCH
- Brott I., et al., 2011, A&A, 530, A115
- Canto J., Raga A. C., Wilkin F. P., 1996, ApJ, 469, 729
- Draine B. T., Salpeter E. E., 1979, ApJ, 231, 77
- García-Arredondo F., Henney W. J., Arthur S. J., 2001, ApJ, 561, 830

- Gull T. R., Sofia S., 1979, ApJ, 230, 782  
 Henney W. J., Arthur S. J., 1998, AJ, 116, 322  
 Henney W. J., O'Dell C. R., 1999, AJ, 118, 2350  
 Henney W. J., Arthur S. J., Williams R. J. R., Ferland G. J., 2005, ApJ, 621, 328  
 Hindmarsh A. C., 1983, IMACS Transactions on Scientific Computation, 1, 55  
 Jones E., Oliphant T., Peterson P., et al., 2001–2018, SciPy: Open source scientific tools for Python, <http://www.scipy.org/>  
 Krtička J., 2014, A&A, 564, A70  
 Lamers H. J. G. L. M., Cassinelli J. P., 1999, Introduction to Stellar Winds. Cambridge, UK: Cambridge University Press  
 Lamers H. J. G. L. M., Snow T. P., Lindholm D. M., 1995, ApJ, 455, 269  
 Landau L., Lifshitz E., 1976, Mechanics, 3rd edn. Course of Theoretical Physics S Vol. 1, Butterworth-Heinemann  
 Mac Low M.-M., van Buren D., Wood D. O. S., Churchwell E., 1991, ApJ, 369, 395  
 Meyer D. M.-A., Mackey J., Langer N., Gvaramadze V. V., Mignone A., Izzard R. G., Kaper L., 2014, MNRAS, 444, 2754  
 Meyer D. M.-A., van Marle A.-J., Kuiper R., Kley W., 2016, MNRAS, 459, 1146  
 Meyer D. M.-A., Mignone A., Kuiper R., Raga A. C., Kley W., 2017, MNRAS, 464, 3229  
 O'Dell C. R., Wen Z., 1994, ApJ, 436, 194  
 Ochsendorf B. B., Tielens A. G. G. M., 2015, A&A, 576, A2  
 Ochsendorf B. B., Cox N. L. J., Krijt S., Salgado F., Berné O., Bernard J. P., Kaper L., Tielens A. G. G. M., 2014a, A&A, 563, A65  
 Ochsendorf B. B., Verdolini S., Cox N. L. J., Berné O., Kaper L., Tielens A. G. G. M., 2014b, A&A, 566, A75  
 Osokinova L. M., Todt H., Ignace R., Brown J. C., Cassinelli J. P., Hamann W.-R., 2011, MNRAS, 416, 1456  
 Osterbrock D. E., Ferland G. J., 2006, Astrophysics of gaseous nebulae and active galactic nuclei, second edn. Sausalito, CA: University Science Books  
 Prinja R. K., 1989, MNRAS, 241, 721  
 Puls J., Vink J. S., Najarro F., 2008, A&ARv, 16, 209  
 Rodríguez-Ramírez J. C., Raga A. C., 2016, MNRAS, 460, 1876  
 Sexton R. O., Povich M. S., Smith N., Babler B. L., Meade M. R., Rudolph A. L., 2015, MNRAS, 446, 1047  
 Spitzer L., 1978, Physical processes in the interstellar medium. New York: Wiley-Interscience  
 Sternberg A., Hoffmann T. L., Paulydrach A. W. A., 2003, ApJ, 599, 1333  
 Tarango Yong J. A., Henney W. J., 2018, MNRAS, in preparation  
 Tenorio-Tagle G., 1979, A&A, 71, 59  
 Vink J. S., de Koter A., Lamers H. J. G. L. M., 1999, A&A, 350, 181  
 Vink J. S., de Koter A., Lamers H. J. G. L. M., 2000, A&A, 362, 295  
 Wilkin F. P., 1996, ApJ, 459, L31  
 de Jager C., Nieuwenhuijzen H., van der Hucht K. A., 1988, A&AS, 72, 259  
 van Buren D., McCray R., 1988, ApJ, 329, L93  
 van Marle A. J., Meliani Z., Keppens R., Decin L., 2011, ApJ, 734, L26

## APPENDIX A: CLOUDY MODELS OF DUST CHARGING AROUND OB STARS

## APPENDIX B: EQUATIONS OF MOTION FOR GRAINS WITH RADIATION AND GAS DRAG

To find the dust grain trajectories  $R_d(\theta)$  in the presence of radiation and drag forces (§ 3.2), we numerically integrate the equations of motion. We define dimensionless cylindrical polar coordinates,

$$(X, Y) = \left( \frac{R_d(\theta) \cos \theta}{R_0}, \frac{R_d(\theta) \sin \theta}{R_0} \right), \quad (\text{B1})$$

and dust grain velocities,

$$(U, V) = \left( \frac{\mathbf{v}_d \cdot \hat{\mathbf{x}}}{v_\infty}, \frac{\mathbf{v}_d \cdot \hat{\mathbf{y}}}{v_\infty} \right), \quad (\text{B2})$$

where  $\hat{\mathbf{x}}$  and  $\hat{\mathbf{y}}$  are unit vectors along the  $X$  and  $Y$  axes (parallel and perpendicular, respectively, to the symmetry axis). The grain equation of motion then follows from equations (37, 38, 42–44) as the following set of coupled differential equations:

$$\begin{aligned} \frac{dX}{dt} &= U & \frac{dY}{dt} &= V \\ \frac{dU}{dt} &= \frac{1}{2} \left[ X \left( X^2 + Y^2 \right)^{-3/2} - a_{\text{drag}}^2 D_1 (U - U_1) \right] \\ \frac{dV}{dt} &= \frac{1}{2} \left[ Y \left( X^2 + Y^2 \right)^{-3/2} - a_{\text{drag}}^2 D_1 (V - V_1) \right], \end{aligned} \quad (\text{B3})$$

where  $(U_1, V_1)$  are the components of the gas velocity (assumed fixed), given by

$$(U_1, V_1) = \begin{cases} \text{parallel stream} & (-1, 0) \\ \text{divergent stream} & \left( \frac{X - \mu^{-1}}{R_1}, \frac{Y}{R_1} \right), \end{cases} \quad (\text{B4})$$

where

$$R_1 = \left( (X - \mu^{-1})^2 + Y^2 \right)^{1/2} \quad (\text{B5})$$

is the distance from the second source, located at  $(X, Y) = (\mu^{-1}, 0)$ . The dimensionless gas density,  $D_1$ , normalized by the value at  $(X, Y) = (1, 0)$ , is

$$D_1 = \begin{cases} \text{parallel stream} & 1 \\ \text{divergent stream} & \frac{(\mu^{-1} - 1)^2}{R_1^2}. \end{cases} \quad (\text{B6})$$

Equations (B3) are integrated using the python wrapper `scipy.integrate.odeint` to the Fortran ODEPACK library (Hindmarsh 1983; Jones et al. 2018), with results shown in Figure 10 for parallel-stream cases and Figure B1 for divergent-stream cases.

## APPENDIX C: FURTHER DETAILS ON IONIZATION FRONT TRAPPING

This appendix will probably be dropped from the paper. It contains details of the derivation of the ionization front trapping that I now think are too verbose to be included, given that this is not the main point of the paper. They are collected here for completeness.

We wish to calculate whether the star is capable of photoionizing the entire bow shock shell, or whether the ionization front will be trapped within it. The number of hydrogen recombinations<sup>18</sup> per unit time per unit area in a fully ionized shell is

$$\mathcal{R} = \alpha_B n_{\text{sh}}^2 h_{\text{sh}}, \quad (\text{C1})$$

while the flux of hydrogen-ionizing photons ( $h\nu > 13.6$  eV) incident on the inner edge of the shell is

$$\mathcal{F} = \frac{S}{4\pi R_0^2}, \quad (\text{C2})$$

where  $S$  is the ionizing photon luminosity of the star. Any shell with  $\mathcal{R} > \mathcal{F}$  cannot be entirely photoionized by the star, and so must have trapped the ionization front. The column density of the shocked shell

<sup>18</sup> The diffuse field is treated in the on-the-spot approximation, assuming all emitted Lyman continuum photons are immediately re-absorbed locally, so the case B recombination co-efficient,  $\alpha_B = 2.6 \times 10^{-13} T_4^{-0.7} \text{ cm}^3 \text{ s}^{-1}$ , is used, where  $T_4 = T/10^4$  K.

can be found, for example, from equations (10) and (12) of Wilkin (1996) in the limit  $v_\infty/V \rightarrow 0$  (Wilkin's parameter  $\alpha$ ) and  $\theta \rightarrow 0$ . This yields

$$n_{\text{sh}} h_{\text{sh}} = \frac{3}{4} n R_0. \quad (\text{C3})$$

Assuming strong cooling behind the shock,<sup>19</sup> the shell density is  $n_{\text{sh}} = M_0^2 n$ , where  $M_0 = v_\infty/c_s$  is the isothermal Mach number of the external stream.<sup>20</sup> Putting these together with equations (3) and (9), one finds that  $\mathcal{R} > \mathcal{F}$  implies

$$x^3 \tau_* > \frac{4 S c_s \bar{m}^2 \kappa}{3 \alpha L}. \quad (\text{C4})$$

From equation (10), it can be seen that  $x$  depends on the external stream parameters,  $n$ ,  $v_\infty$  only via  $\tau_*$ , and so equation (23) is a condition for  $\tau_*$ . In the radiation bow shock case,  $x = (1 + \eta)^{1/2}$ , and the condition can be written:

$$\tau_* > 145.0 \frac{S_{49} T_4^{1.7} \kappa_{600}}{L_4 (1 + \eta)^{3/2}}, \quad (\text{C5})$$

where

$$S_{49} = S / (10^{49} \text{ s}^{-1}).$$

Numerical values of  $S_{49}$  for our three example stars are given in Table 1. In the radiation bow wave case,  $x = 2\tau_*$ , and the condition can be written:

$$\tau_* > \left( 18.1 \frac{S_{49} T_4^{1.7} \kappa_{600}}{L_4} \right)^{1/4}, \quad (\text{C6})$$

$\tau_* \sim n^{1/2}/v_\infty$  This simple criterion is shown by the dark red line in Figure 2. If  $n/v_{10}^2 > 1000$  to 5000, depending only weakly on the stellar parameters, then the outer parts of the shocked shell are neutral, instead of ionized.

Assuming photoionization equilibrium, the hydrogen photoabsorption optical depth of the shell is

$$\tau_{\text{gas}} = -\ln(1 - \mathcal{R}/\mathcal{F}), \quad (\text{C7})$$

so long as  $\mathcal{R} < \mathcal{F}$ .

We will assume a typical photoionized temperature of 8000 K, so that  $c_s \approx 10 \text{ km s}^{-1}$  and  $M_0 = v_{10}$ , yielding

$$\tau_{\text{gas}} = -\ln(1 - 8.42 \times 10^{-6} v_{10}^2 n^2 R_{0,\text{pc}}^3 S_{49}^{-1}), \quad (\text{C8})$$

where

$$R_{0,\text{pc}} = R_0 / (1 \text{ pc})$$

The dust opacity is approximately constant at FUV to EUV wavelengths, so the dust optical depth of the shocked shell to ionizing photons follows from equations (8) and (21) as  $\tau_d = \frac{3}{8} \tau$ .

The hydrogen ionization fraction,  $y$ , at the outer edge of the shocked shell then follows as

$$\frac{y^2}{1 - y} = \frac{\sigma \mathcal{F}}{\alpha_B n} e^{-(\tau_d + \tau_{\text{gas}})}, \quad (\text{C9})$$

where  $\sigma$  is the effective hydrogen photoionization cross section, averaged over the local ionizing spectrum. Since the frequency-dependent

<sup>19</sup> This is shown to be justified in § 2.1.3.

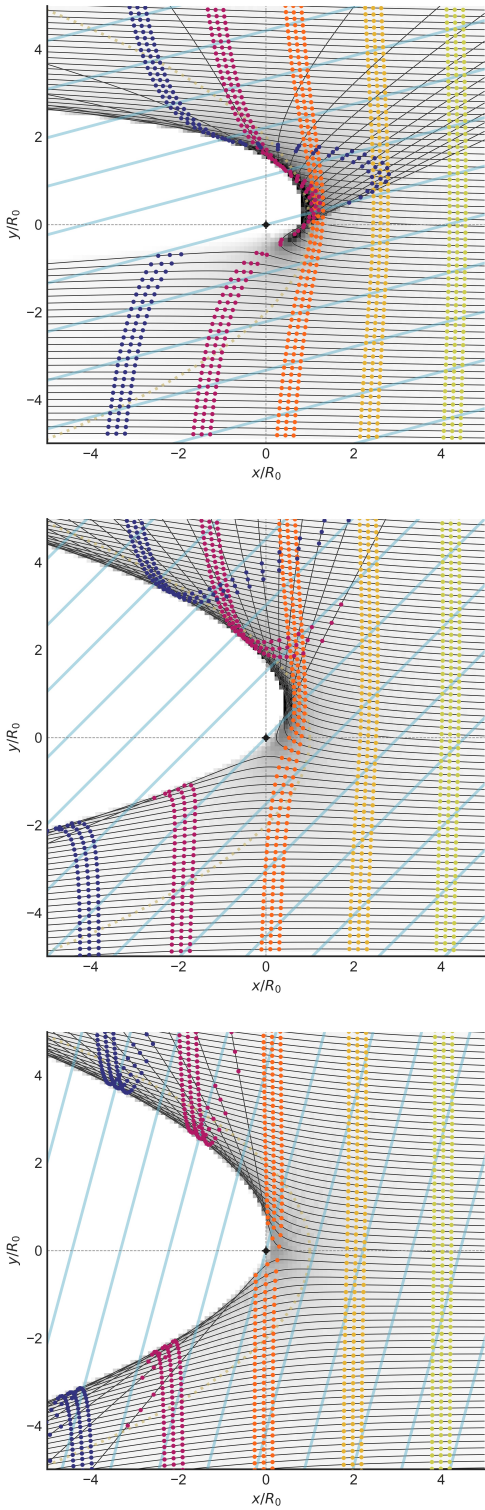
<sup>20</sup> The sound speed depends on the temperature and hydrogen and helium ionization fractions,  $y$  and  $y_{\text{He}}$  as  $c_s^2 = (1 + y + z_{\text{He}} y_{\text{He}})(kT/\bar{m})$ , where  $z_{\text{He}}$  is the helium nucleon abundance by number relative to hydrogen and  $k = 1.380\,650\,3 \times 10^{-16} \text{ erg K}^{-1}$  is Boltzmann's constant. We assume  $y = 1$ ,  $y_{\text{He}} = 0.5$ ,  $z_{\text{He}} = 0.09$ , so that  $c_s = 11.4 T_4^{1/2} \text{ km s}^{-1}$ .

cross section,  $\sigma_\nu \sim \nu^{-3}$ , is strongly peaked at the threshold, the local EUV spectrum becomes harder with increasing  $\tau_{\text{gas}}$ , as the lower frequency photons are selectively absorbed,<sup>21</sup> leading to a reduction in the effective  $\sigma$ . An approximate fit to the results in Appendix A of Henney et al. (2005) is

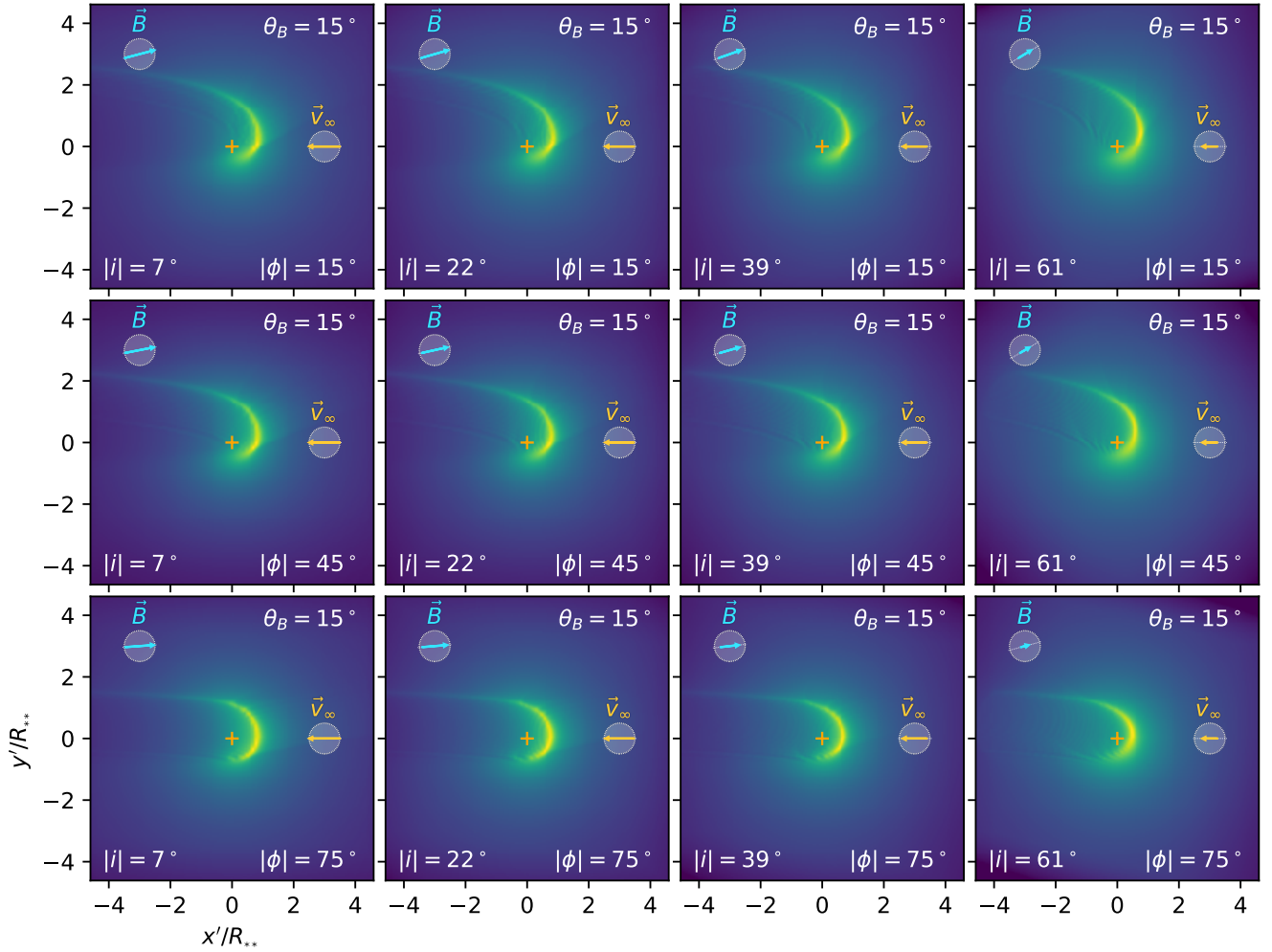
$$\sigma = 0.5 \sigma_0 e^{-\tau_{\text{gas}}/3} \quad (\text{C10})$$

where  $\sigma_0 = 6 \times 10^{-18} \text{ cm}^2$  is the threshold cross-section. Although this was derived for a particular ionizing spectrum (40 000 K black body), we adopt it for all our hot stars.

This paper has been typeset from a  $\text{TeX}/\text{LaTeX}$  file prepared by the author.



**Figure 11.** Grain trajectories for magnetised dust waves in the limit of no gas drag and small gyro-radius.

**Figure 12.** xxx

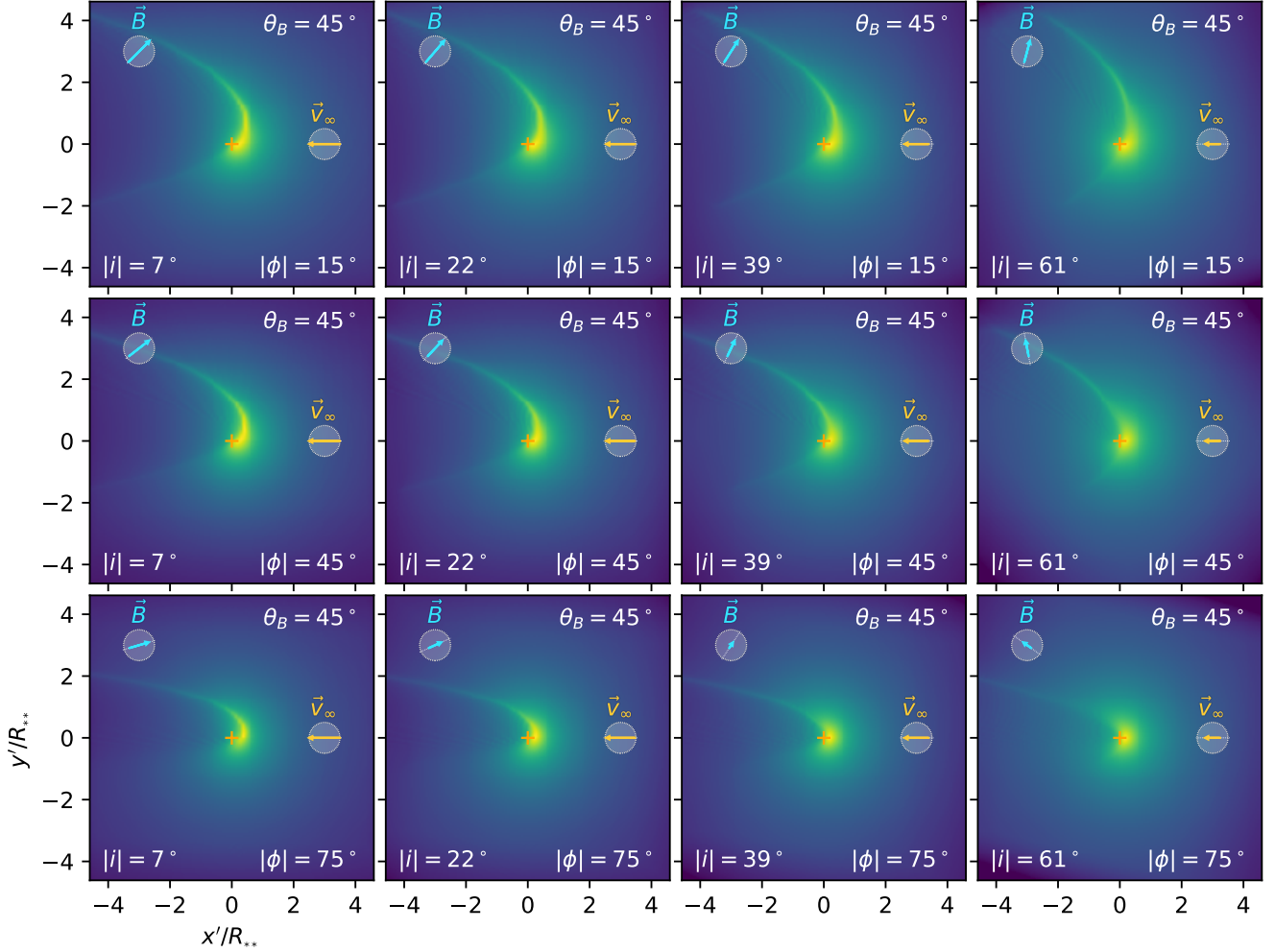
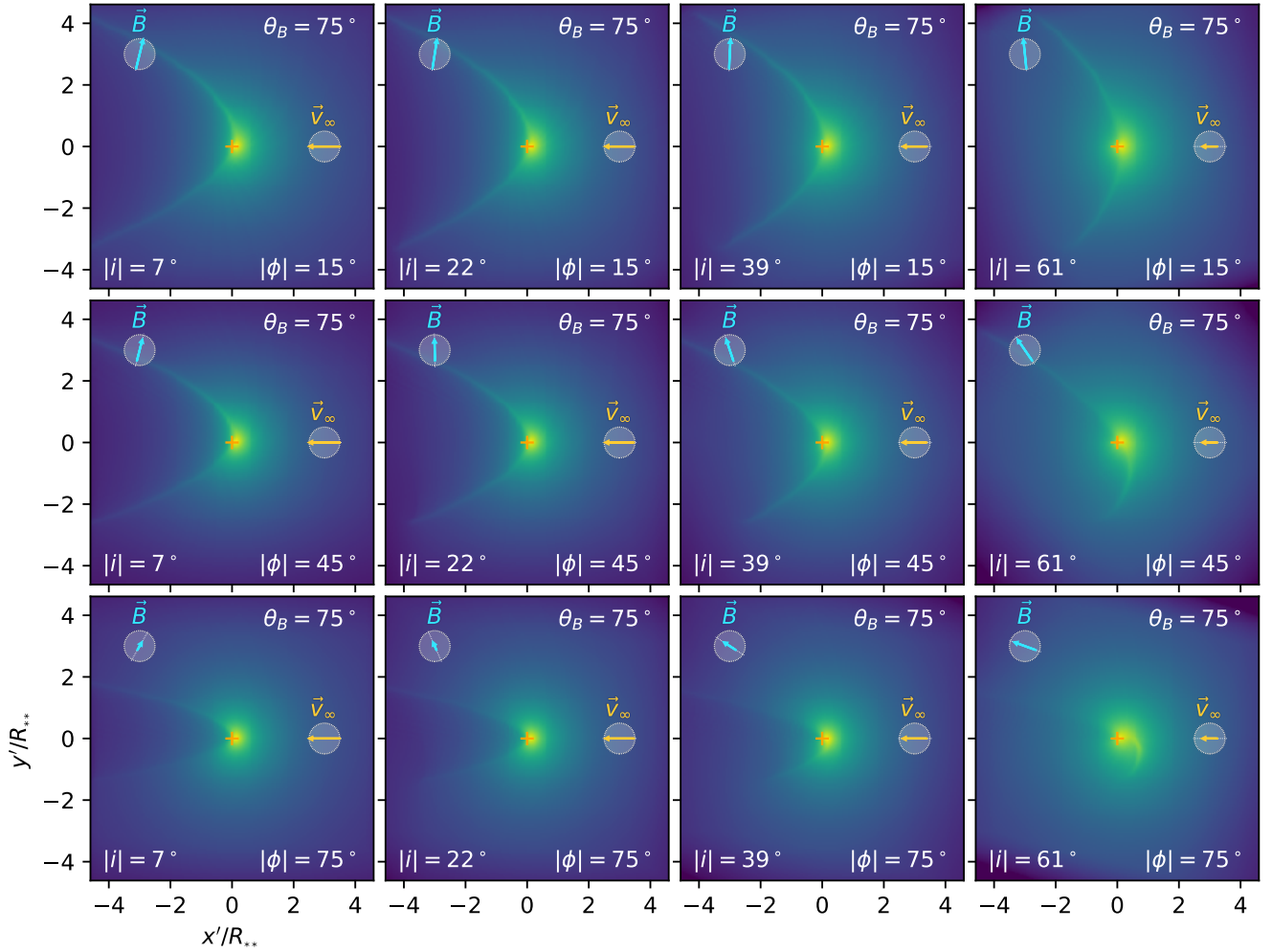
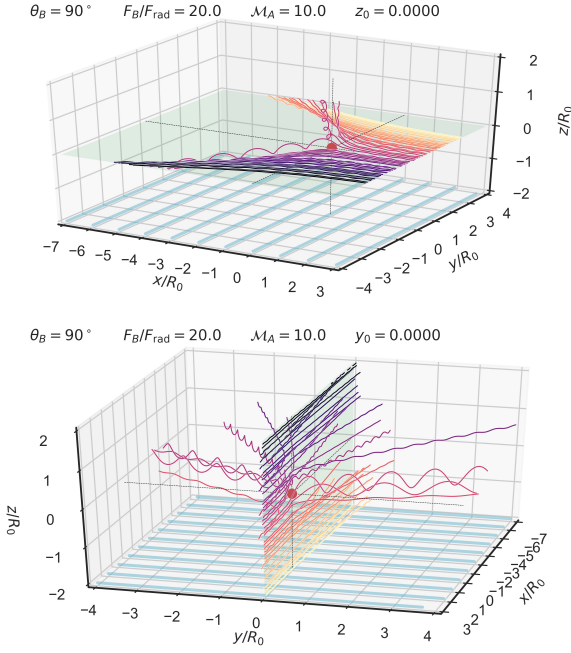
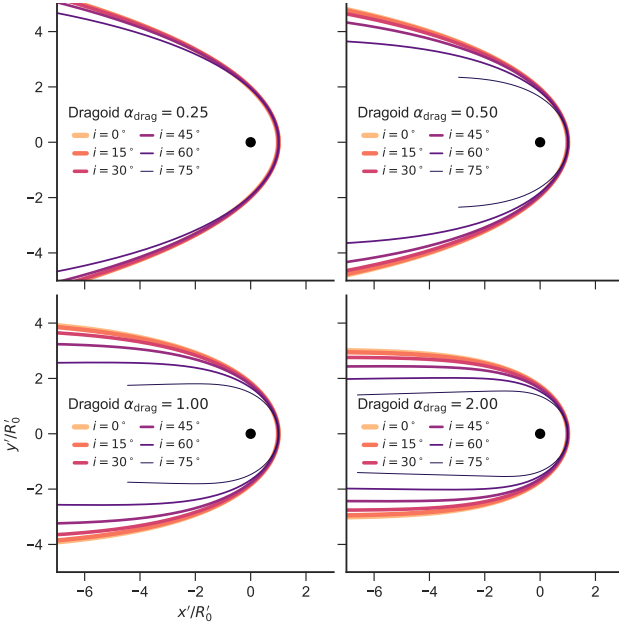


Figure 13. xxx

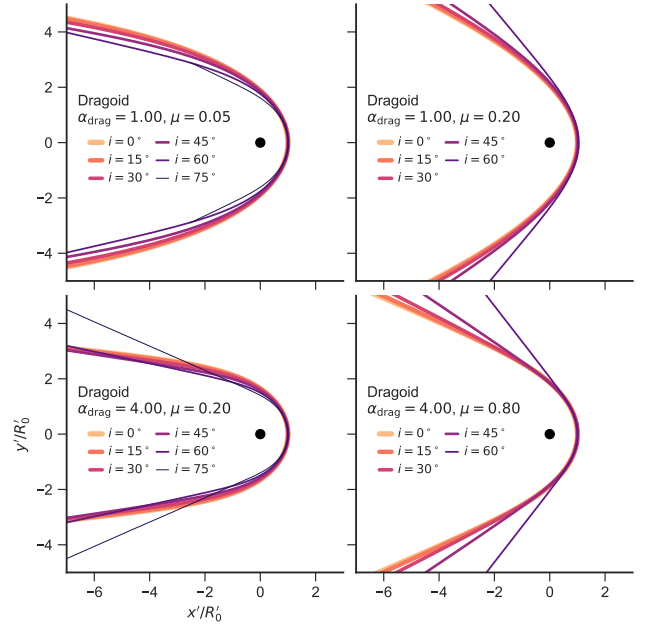
**Figure 14.** xxx



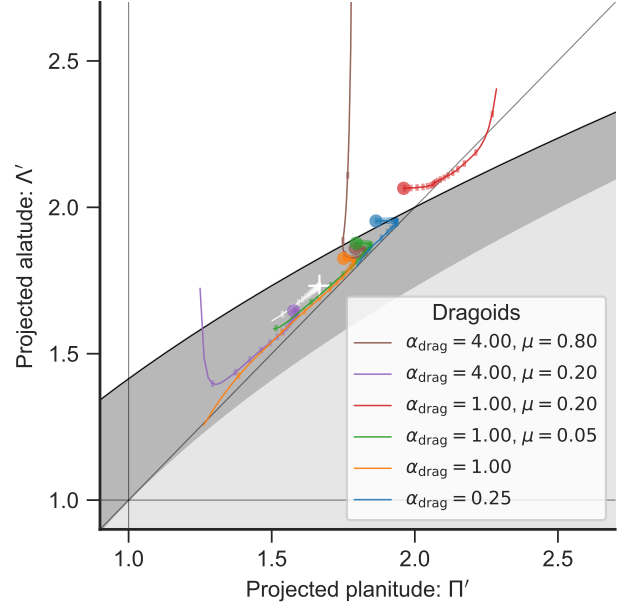
**Figure 15.** Streamlines in three dimensions of resolved gyro-radius



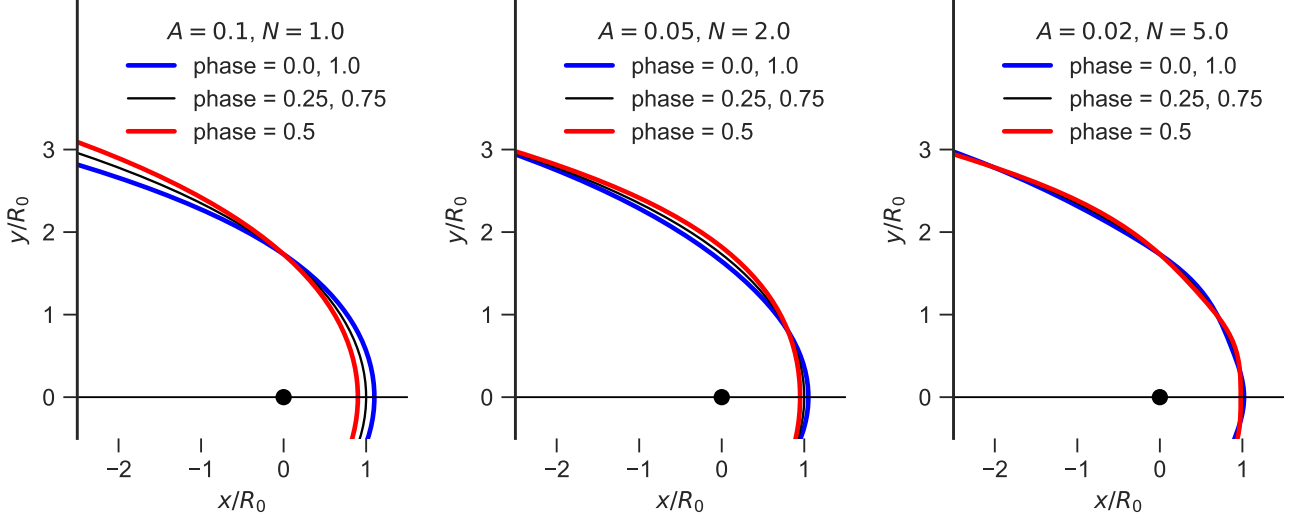
**Figure 16.** Apparent bow shapes in the plane of the sky for parallel-stream dragoids as a function of inclination angle. Drag coefficient,  $\alpha_{\text{drag}}$  increases from top-left to bottom-right. Inclination  $|i|$  is shown in  $15^\circ$  increments, indicated by line color and thickness (see key).



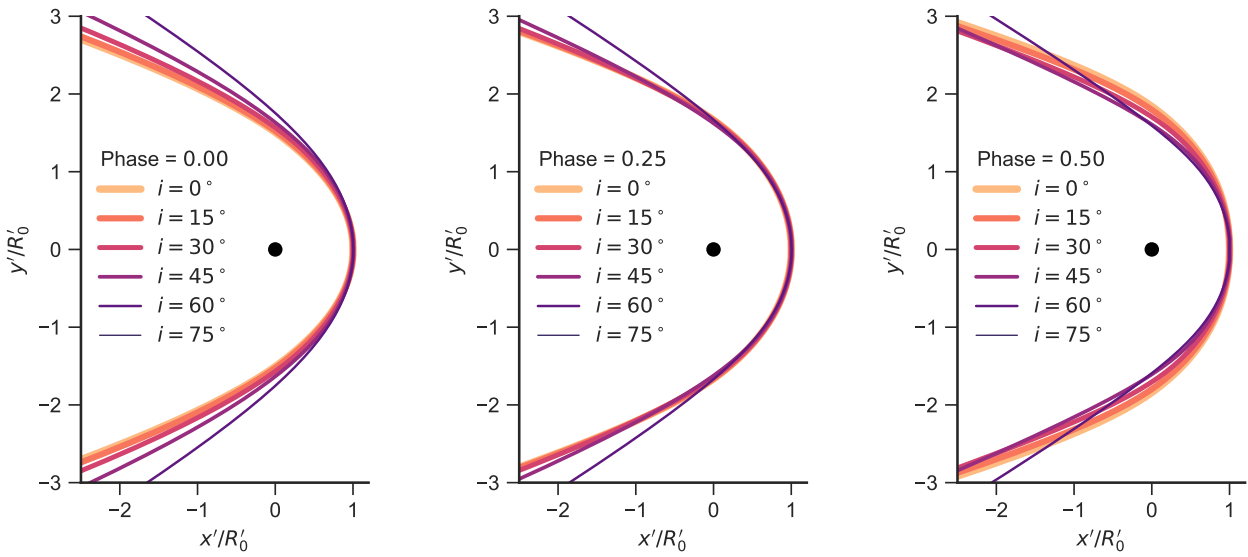
**Figure 17.** As Fig. 16 but for divergent stream dragoids. Drag coefficient increases from top to bottom, while degree of divergence increases from left to right.



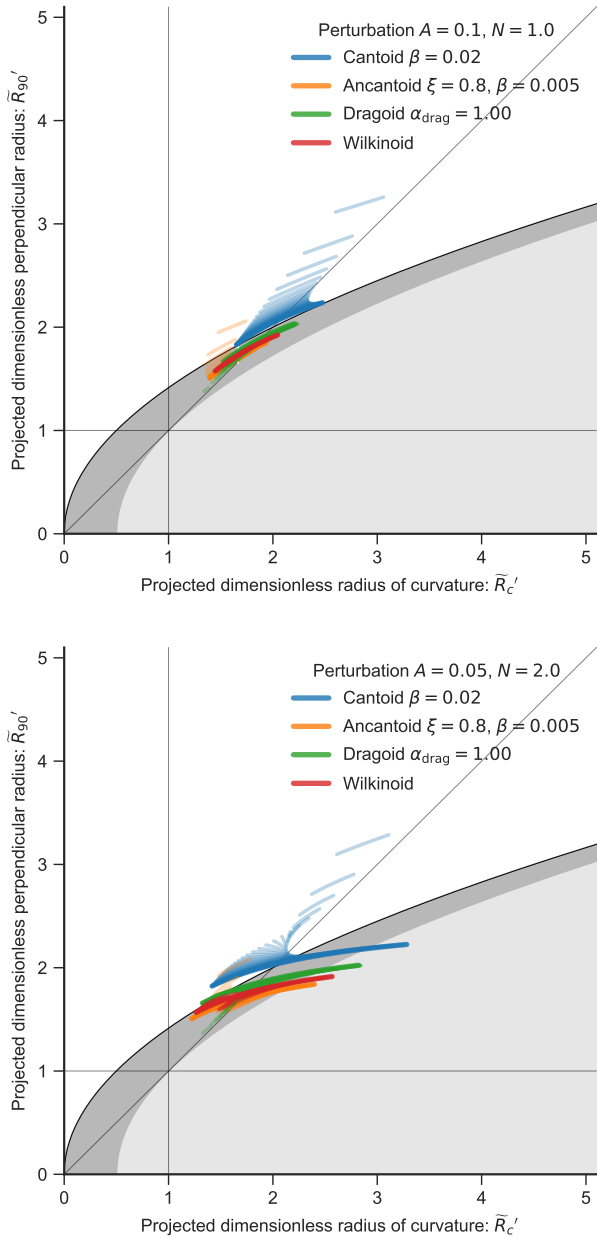
**Figure 18.** Apparent projected shapes of dragoids in the  $\Pi'$ – $\Lambda'$  plane. Colored symbols indicate the  $|i| = 0$  position for selected models (see key). Thin lines show the inclination-dependent tracks of each model, with tick marks along each track for 20 equal-spaced values of  $|\sin i|$ . Gray shaded regions are as in Fig. 11a of Paper I. The wilkinoid track is shown in white.



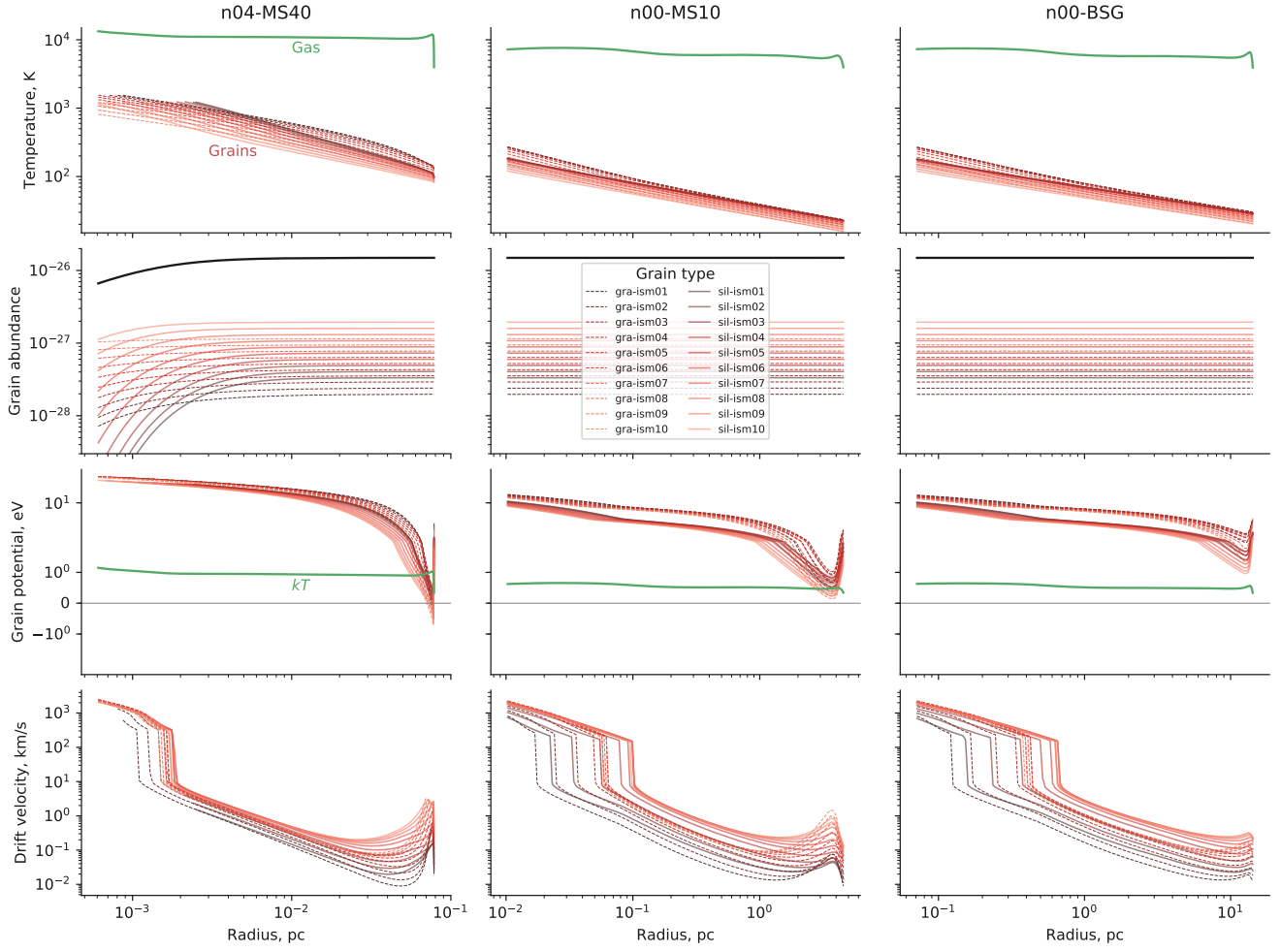
**Figure 19.** Small-amplitude standing wave perturbations to wilkinoid bow shapes. The maximum deviations from the base shape are seen at phases  $\phi = 0$  (blue line) and  $\phi = 0.5$  (red line), while the perturbation is zero at  $\phi = 0.25$  and  $0.75$  (black line). Results are shown left to right for increasing wave numbers  $N$  and decreasing amplitudes  $A$ : (a)  $A = 0.1$ ,  $N = 1.0$ , (b)  $A = 0.05$ ,  $N = 2.0$ , (c)  $A = 0.02$ ,  $N = 5.0$ .



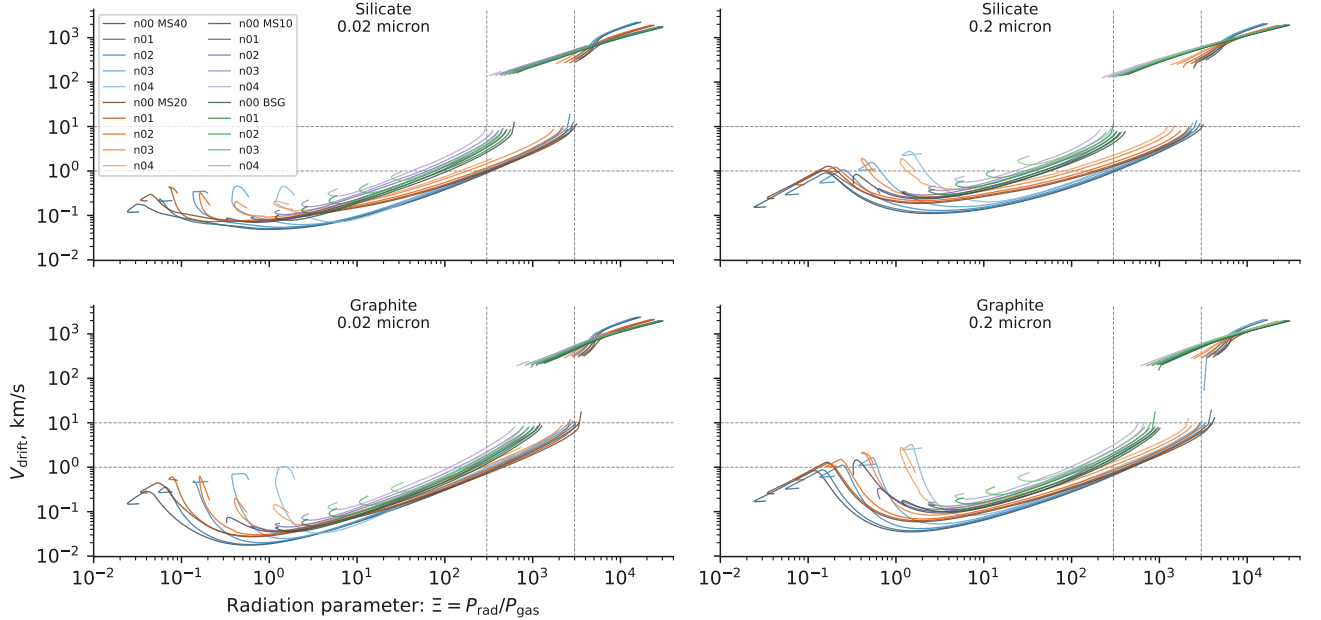
**Figure 20.** Plane-of-sky projections of perturbed bow shapes. In all cases, the base bow shape is ancantoid with  $\xi = 0.8$ ,  $\beta = 0.005$  and the perturbation is the same as in the central panel of Fig. 19, with amplitude  $A = 0.05$  and wave number  $N = 2.0$ . Results are shown for inclination angles  $i = 0$  to  $i = 75^\circ$  (indicated by line color and thickness, see key) and for different fractional phases of the oscillation: (a)  $\varphi = 0.0$ , (b)  $\varphi = 0.25$ , (c)  $\varphi = 0.50$ . Unlike in Fig. 19, the spatial coordinates are normalized to the instantaneous projected apex radius  $R'_0$  at each phase, so the apex does not appear to move.



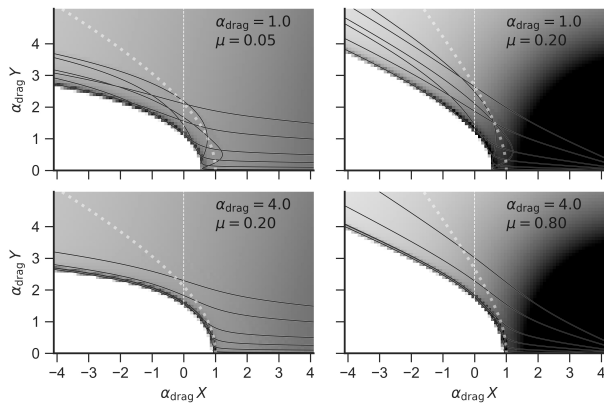
**Figure 21.** Diagnostic diagram for perturbed shapes



**Figure A1.** Dust properties as a function of radius from star for three selected Cloudy models. (a)  $40 M_{\odot}$  main-sequence star in medium of density  $10^4 \text{ cm}^{-2}$ . (b)  $10 M_{\odot}$  main-sequence star in medium of density  $1 \text{ cm}^{-2}$ . (c) Blue supergiant star in medium of density  $1 \text{ cm}^{-2}$



**Figure A2.** Drift velocity versus radiation parameter  $\Xi_P$ . Each line represents a model with ambient density and stellar type as indicated in the key.

**Figure B1.** Divergent dragoids